D3.2 | Readout implementation

Author(s): Zhuoran Geng, Ari Helenius, Ilari Maasilta, Florence Levy-Bertrand, Alessandro Monfardini

Delivery date: 23.11.2021

Version: 2.0

This project has received funding from the European Union's Horizon 2020 research and innovation programme under grant agreement No 800923.

Project Acronym:	SUPERTED
Project Full Title:	Thermoelectric detector based on superconductor-ferromagnet heterostructures
Call:	H2020-FETOPEN-2016-2017
Topic:	FETOPEN-01-2016-2017
Type of Action:	RIA
Grant Number:	800923
Project URL:	https://superted-project.eu/

Editor:	Ilari Maasilta, University of Jyväskylä
Deliverable nature:	Report (R)
Dissemination level:	Public (PU)
Contractual Delivery Date:	31.11.2021
Actual Delivery Date:	23.11.2021
Number of pages:	38
Keywords:	calorimeter, bolometer, read-out, SQUID
Author(s):	Ari Helenius, University of Jyväskylä Zhuoran Geng, University of Jyväskylä Ilari Maasilta, University of Jyväskylä Florence Levy-Bertrand, Institut Néel, Grenoble Alessandro Monfardini, Institut Néel, Greoble
Contributor(s):	Tero Heikkilä, University of Jyväskylä Sanna Rauhamäki, University of Jyväskylä
External contributor(s):	Ioan Pop, Karlsruhe Institute of Technology Patrik Baluch, Karlsruhe Institute of Technology

Abstract

This Deliverable 3.2 '*Read-out implementation*' is a summary of the project's results for the implementation of the read-out circuit for thermoelectric detectors. The aim of Work Package 3 is to

This project has received funding from the European Union's Horizon 2020 research and innovation programme under grant agreement No 800923.

demonstrate and characterize FI/S based systems with antennas (THz, continuum) or heavy-metal absorbers (X-ray, single events) as detectors of electromagnetic radiation in two distinct frequency regimes. The deliverable first describes progress with the current read-out with a Superconducting Quantum Interference Device (SQUID) amplifier, concentrating on the cryogenics, wiring and the details of the SQUID amplifier setup, including characterization. Second, progress toward the implementation of a highly multiplexable alternative readout based on kinetic inductance detectors (KIDs) is detailed.

This project has received funding from the European Union's Horizon 2020 research and innovation programme under grant agreement No 800923.

1. Introduction

The main aim of Work Package 3 (WP 3) is to demonstrate and characterize superconductor-ferromagnet thermoelectric systems with antennas (THz, continuum) or heavy-metal absorbers (X-ray, single events) as detectors of electromagnetic radiation in two distinct frequency regimes. A practical realization of such a superconductor-ferromagnet thermoelectric detector (SFTED) requires sensitive amplification of the output signal of the device. In the previous report D3.1 Read-out schemes, we discussed the options how to design the amplifier chains, with a conclusion that a superconducting quantum interference device (SQUID) readout is feasible for the readout. The main results of that study are also published in Ref. [1]. The purpose of this deliverable is to report the practical steps taken to implement and test a SQUID readout. Parallel to that avenue, we also report the progress with an alternative technology based on kinetic inductance detector (KID) readout. Chapter 2 first describes the developed cryogenic setup for the detectors, after which chapter 3 discusses the details about the measurement setup, in other words details about the SQUID electronics. The SQUID electronics components, both the low temperature and the room temperature stages, were ordered from a commercial vendor, Magnicon GmbH, already in spring 2020. Due to serious pandemic related delays and problems in their production, the company failed to meet its promised delivery time, leading to a delay of this deliverable. Currently, we have obtained and installed the room temperature electronics from them, but still have not received the actual SQUID chip. However, we have implemented a backup plan, and purchased another SQUID amplifier chip from a different vendor (Star Cryoelectronics LLC). We installed it successfully and demonstrated its performance and compatibility with the room temperature electronics, as will be shown later in this report in Chapter 3. Chapter 4 discusses near future practical steps to be taken for the SQUID readout implementation, whereas Chapter 5 details the KID readout designs and practical progress, with conclusions drawn in Chapter 6.

2. Cryogenic setup for SUPERTED detectors

To allow for sub-100 mK operational temperature of the detector for low noise and thus better performance characteristics, we have decided to use a He3/He4 dilution refrigerator at JyU as the cryogenic cooling technology. For the SFTED X-ray calorimeter we will use an in-house made non-commercial plastic dilution refrigerator (PDR)[2] designed and modified for the needs of this project, to reach the needed temperatures. Such a refrigerator model can reach a base temperature below 50 mK, which is adequate for the performance goals set for the project. Its temperature is also easily tunable up to 1 K range for testing of the temperature dependence. One of the main strengths of the PDR refrigerator and the reason why we have chosen it as the cryogenic platform is that it has a faster turn-around time between cooldowns than a standard commercial high power dilution refrigerator, which is highly valuable feature in a development project such as this.

This project has received funding from the European Union's Horizon 2020 research and innovation programme under grant agreement No 800923.

The basic principle of a PDR dilution refrigerator is to have an ambient temperature produced by liquid helium (LHe) bath at 4.2K, which surrounds the active parts of the refrigerator. In practice, this LHe bath is maintained inside a transport Dewar, which is optimized for low LHe boil-off, allowing cost-effectiveness and, if necessary, week-long experimentation without the need of further LHe transfers. The active parts of the refrigerator then further decrease the temperature at different stages of the refrigerator body first to 1.5 K and then to the base temperature ~50 mK. A sample stage thermally couples with the 50 mK refrigerator stage, to allow for installation of the detector and the low-temperature SQUID amplifier. In the following sections, the different stages of the cryostat will be shown and discussed in more detail to give insight into the performance, methods, problems and solutions of the setup. These include for example questions on magnetic and electrical shielding, thermalization and measures against electromagnetic pickup.

2.1 Thermalization and temperature stabilization

In dilution refrigeration, by pumping and circulating He3 across a phase boundary between He3 rich and He3 dilute mixtures of He3/He4 liquid, we can cool the region where most of the mixture resides (the so-called mixing chamber) to the base temperature of approximately 50 mK. However, many different stages are needed for pre-cooling. A schematic and a photograph of the bottom part of the JYU PDR dilution refrigerator for SUPERTED are shown in Fig. 2.1. What is not shown are the pumping lines that extend upwards to the room temperature flange. The figure shows what is inside the vacuum jacket (vacuum jacket not shown). It is in direct contact with the LHe bath at 4 K, thus the vacuum inside isolates the inside parts thermally from 4 K to allow lower temperatures. The flange shown below (1) forms the top flange of the vacuum jacket and is thus the 4 K flange. By pumping a smaller volume of liquid helium in a stage below the 4 K flange in the 1.5 K pot shown by (2), the Cu stage thermalized with the pot reaches a temperature of around 1.5 K. The pot replenishes LHe from the main bath with a siphon tube (1), whose flow rate is designed to match the pumping rate so that the LHe level in the pot stays stable. Below the 1.5K stage is the so-called plastic part, number (3), which contains the tubes and volumes for the He3/He4 mixture used to reach the base temperature. The top of the plastic part houses the still chamber at 0.7 K, the bottom the mixing chamber at base temperature, and the main body the continuous heat exchanger between the incoming and outgoing mixtures. It is made from a plastic material which can be machined well, survives repeated thermal cycling and which has a low thermal conductivity (Stycast). The experimental Cu+Al sample stage housing both the SQUID and the detector connects directly with the cold mixture with the help of a large effective surface area silver part to improve thermal coupling.

Temperature fluctuations in the cryogenic setup could introduce noise to the detector measurements. To keep the temperature stable, multiple thermal buffers are utilized at different temperature levels in our cryostat. As outlined above, it has effectively four layers of thermalization and thermal buffers to reach and stabilize the base temperature: The 4 K bath of liquid helium, where most of the external thermal fluctuation sources can be dissipated, the 1.5 K flange of the pot with a large thermal mass

This project has received funding from the European Union's Horizon 2020 research and innovation programme under grant agreement No 800923.

due to the copper body, the still mixture volume at 0.7 K, and finally the sample stage which has a significantly larger thermal mass (Cu parts) compared to the SQUID and detector chips, producing a stable enough temperature bath for the measurement.

The wiring of the cryostat also follows similar thermalization. All wiring is first thermalized to 4 K temperature at the He layer. Further down, all the wiring is thermalized at the 1.5K pot, still and/or sample stage levels depending on the end point. All measurement wiring has been anchored to the four mentioned thermal buffer stages, which therefore dissipate the excess heat passed down from the higher temperature stages. This is critical for cryogenic setups since the lower temperature stages provide lower cooling power, which in our case is ~ 1 μW at 100 mK.

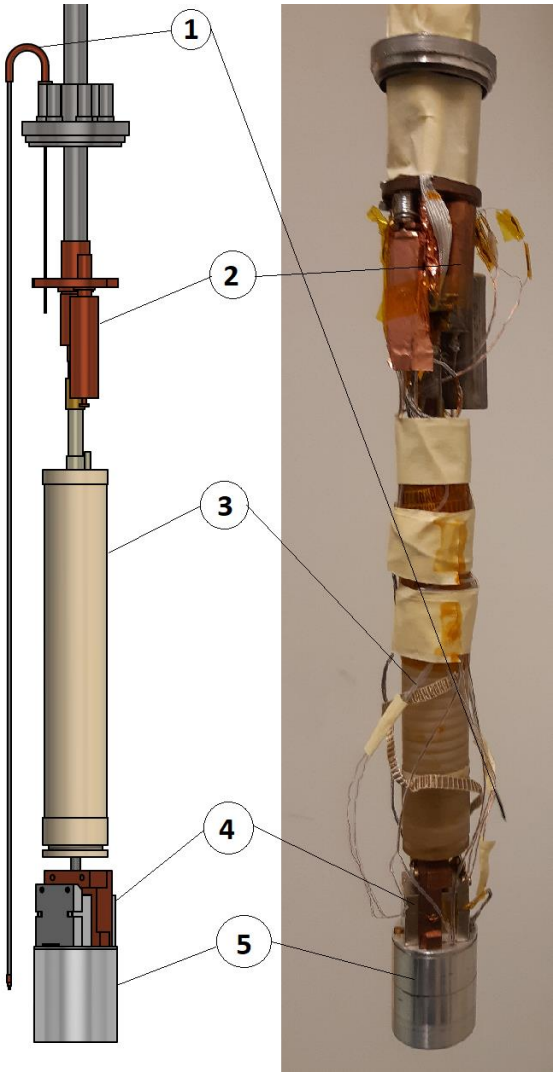

Figure 2.1. Schematic (left) and a photograph (right) of the vacuum jacket innards of the PDR refrigerator. On the left, wiring and small tubing are not shown for clarity. 1: 1.5 K Pot siphon connecting to the 4 K flange at the top of the vacuum jacket. 2: 1K Pot chamber. 3: Plastic part, containing the still heat exchangers and the mixing chamber. 4: SQUID housing, and 5: Sample container (sample stage layer).

This project has received funding from the European Union's Horizon 2020 research and innovation programme under grant agreement No 800923.

2.2 External electric and magnetic interference considerations

The output current of a SUPERTED detector will be measured by a SQUID amplifier as an extremely small change in the magnetic flux. This readout scheme requires paying attention to the electromagnetic (EM) shielding in the cryogenic system. In our setup, EM shielding is implemented with multiple layers of enclosures, in order to reach the desired conditions. First of all, the measurements are carried out in an electromagnetically shielded (EMS) room, acting as a Faraday cage. Cabling from outside the EMS room to inside is done through optical cables to reduce the electrical disturbances from outside of the EMS room. Inside the EMS room, all the technical wiring (thermometer, etc.) and measurement wirings are twisted coaxial (shielded) cables. The room temperature amplifier part of the SQUID electronics is installed inside the EMS room, connecting directly with the cryostat body to minimize excess cabling. The He4 dewar also acts as another Faraday cage for the cabling in the refrigerator. Maybe the most important shielding step implemented, are the magnetic shields installed at the sample stage, as standard non-magnetic materials cannot effectively screen low-frequency magnetic field noise [3], to which the SQUID amplifier is sensitive. We have implemented a two stage shielding, with an outer shield machined from Cryoperm10®[4], which is a Mu-metal with optimized shielding properties (permeability) at low temperatures, and an inner shield made from aluminum (Al-6063), which turns superconducting during the cooldown process. This double shielding ensures that the external magnetic field fluctuation around the SQUID is minimized throughout the measurements. The sample stage design is reviewed in more detail in Section 2.4 below.

2.3 Details on the cryostat wiring

Minimizing the external noise pickup to improve the signal SNR is one key factor when designing the wiring solutions, another one is minimizing the conduction heat load.

Starting with the heat load, all the wiring is thermalized at 4 K to ensure that the true ambient temperature is from the helium bath. Three different types of wirings are used between room temperature and the 4 K flange: resistive Manganin, and Constantan[5] in cases where resistance in the wire can be tolerated, reducing thus the thermal conductivity, and high conducting copper wire for the cases where wire resistance has to be kept low. The constantan loom wire has low-pass filtering added above the vacuum jacket. At the 4 K stage, all high conductive copper wires and some of the manganese wires continue to lower temperature stages as NbTi superconducting wiring, to further reduce the heat dissipation and conduction. Although the dissipation is reduced to zero in NbTi wiring at the frequencies of interest, we note that the wire has a copper matrix, leading to some elevated heat conduction compared to a pure superconductive material. Therefore, the copper matrix in the NbTi wiring has been removed by etching from a length of ~ 5cm, to cut off the heat transport through the matrix.

This project has received funding from the European Union's Horizon 2020 research and innovation programme under grant agreement No 800923.

All the wires which continue down from 4K to the sample stage are thermalized at the 1.5 K stage by either soldered connections in case of NbTi and Mn wires, or by well-designed thermal sink with constantan wiring, where the constantan wire loom is wound directly onto a copper thermal sink and glued with low temperature varnish [6], to increase the effectiveness of the thermal sink.

The wires continuing to 50 mK temperatures, the sample stage, are wound around the plastic part of the cryostat. No disconnections have been made for the Constantan loom between 4K and the base temperature, as it has low enough thermal conductivity. However, it can be disconnected for the measurements with the SQUID readout, if necessary, its purpose is to provide additional wiring for optional DC testing of the devices.

EM interference pick-up can cause problems in wiring, however one effective way against this is to twist a pair of wires together to cancel out contributions of inductive coupling [7]. Pairwise twisting is done for all applicable wiring in all applicable places in the cryostat. Some notable exclusions are the platforms where two wires are connected through a solder post. However, in those regions another method of pick-up protection has been implemented: most of the connection areas are enclosed in shielded boxes, whereas the rest are fully covered by pieces of copper tape around the solder spots.

2.4 Detailed design of the sample stage

The designed and built sample stage provides both a stable magnetic and thermal environment for the SQUID sensor and the SUPERTED detector. The volume of the sample container offers additional benefits for measuring, such as room for an additional coil for local magnetic field tuning, space for the x-ray source and rotation of the sample mount circuit board, or for additional magnetic field protection. The sample stage design is shown up close in Figure 2.2 and the parts list is shown in Table 1. Starting with numbers 1 and 2, which form the Cryoperm10® box and 3 and 4, which form the inner superconducting aluminum shielding box, both components mitigate the changes (noise) of the ambient magnetic field on the SQUID. The Cryoperm10® is placed as the outer shield to prevent flux trapping inside the superconducting box during the cooldown through the critical temperature of Al. Number 5 is a thermalization platform for the SQUID, made of copper. These five parts allow the SQUID to be operated in a low noise, stable environment. The aluminum sample container base, number 6 and detachable lid, number 7, offer similar magnetic field and radiofrequency protection for the samples. The inside surface of the lid is covered with RF absorbing material (Eccosorb) to reduce the effect of stray radiation entering the sample volume. The thermalization platform for the detectors, number 8, is made of copper, which houses the components needed for the sample stage thermal control, i.e. a RuOx thermometer and a heating resistor. Numbers 9 and 10 are circuit boards which are connected by the 15-pin connectors (black), however only two pins are needed for the SUPERTED measurements to connect the detector to the SQUID input. It is the lower board that can be used to mount the detector, by bonding it to the pads of the circuit board. Finally, number 11 are the brass bolts which thermalize the circuit boards and samples into the stage temperature of approximately 50 mK minimum, as they connect the various copper parts to the silver rod that is

This project has received funding from the European Union's Horizon 2020 research and innovation programme under grant agreement No 800923.

finally in direct contact with the cold mixture. The detachable circuit board (sample mount) makes it easy for fast changing of samples and bonding, as one only has to remove one part and two nuts, making the whole system more robust in the long run.

This project has received funding from the European Union's Horizon 2020 research and innovation programme under grant agreement No 800923.

Table 1. Sample stage part list.

Part	Number in Figure 2	Material
Outer SQUID housing lid	1	Cryoperm10®
Outer SQUID housing	2	Cryoperm10®
Inner SQUID housing lid	3	Al-6063
Inner SQUID housing	4	Al-6063
SQUID thermalization	5	Oxygen free Cu
Sample container base	6	Al-6063
Sample container detachable lid	7	Al-6063
Thermal stage	8	Oxygen free Cu
Integrated circuit board for sample stage	9	Si/Cu
Detachable circuit board, sample mount	10	Si/Cu
Brass bolts	11	Brass

This project has received funding from the European Union's Horizon 2020 research and innovation programme under grant agreement No 800923.

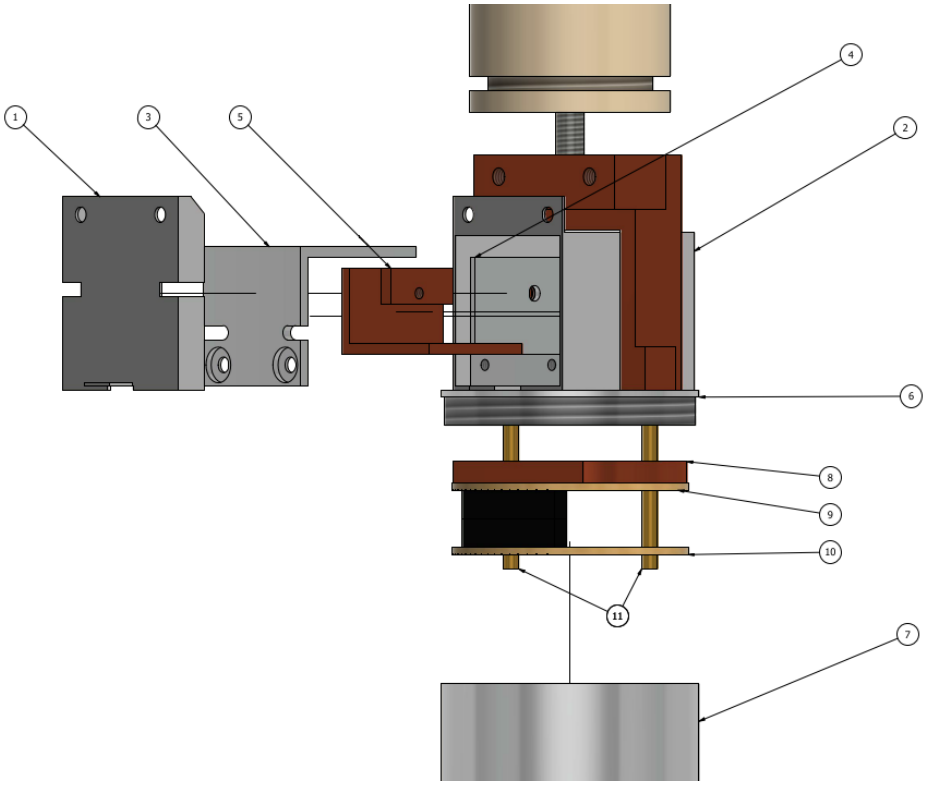

Figure 2.2. Close-up schematic of the sample stage parts, wiring excluded for clarity. 1-2: Cryoperm10® magnetic shields for SQUID housing, 3-4: Aluminum superconducting shield for SQUID housing, 5: SQUID thermalization copper platform, 6-7: Aluminum sample container, 8: sample stage thermal stage, 9-10: sample stage circuit boards with 15-pin connectors, 11: brass bolts for thermalization.

2.5 Magnetic ordering of the ferromagnet inside the sample container

Since the magnetization of the ferromagnetic insulator of a SUPERTED detector is randomly oriented after the fabrication and cannot be permanently polarized at room temperature, a field polarization step (sweeping the field up and down) at low temperatures with an in-plane magnetic field before operation is required. To achieve this possibility, we have designed and built an extra electromagnetic cylindrical coil, to be attached to the sample mount. Finite element method (computed by using Comsol multiphysics ver. 5.5[8]) was used to simulate the magnetic field conditions inside the Al sample container to find a suitable geometry for a superconducting NbTi coil to introduce ordered alignment into the ferromagnetic insulator. In Figure 2.3 the coil geometry is shown with the simulation results using realistic current and the materials in question.

Our conservative simulation shows that a 14 mT magnetic field can be introduced easily using this design with ~100 turns an input current of 2 A. This has been shown by measurements in Pisa to be enough to magnetize FI samples grown at San Sebastian at 4 K. Without further increase in current,

This project has received funding from the European Union's Horizon 2020 research and innovation programme under grant agreement No 800923.

higher magnetic field is achievable up to about a factor of four, by adding the number of turns of the coil, limited by the physical size constraint of the coil.

If a much higher magnetic field is required for characterization purposes, an alternative solution to increase the field further is to rotate the sample stage circuit board 90 degrees and to use an external coil to produce magnetic field. (External coils attached to the vacuum jacket exist, with the field vector pointing perpendicular to the circuit board plane). However, in this case, the magnetization has to be performed before the sample container becomes superconducting, in order to ensure the field penetration (trapping) into the sample container.

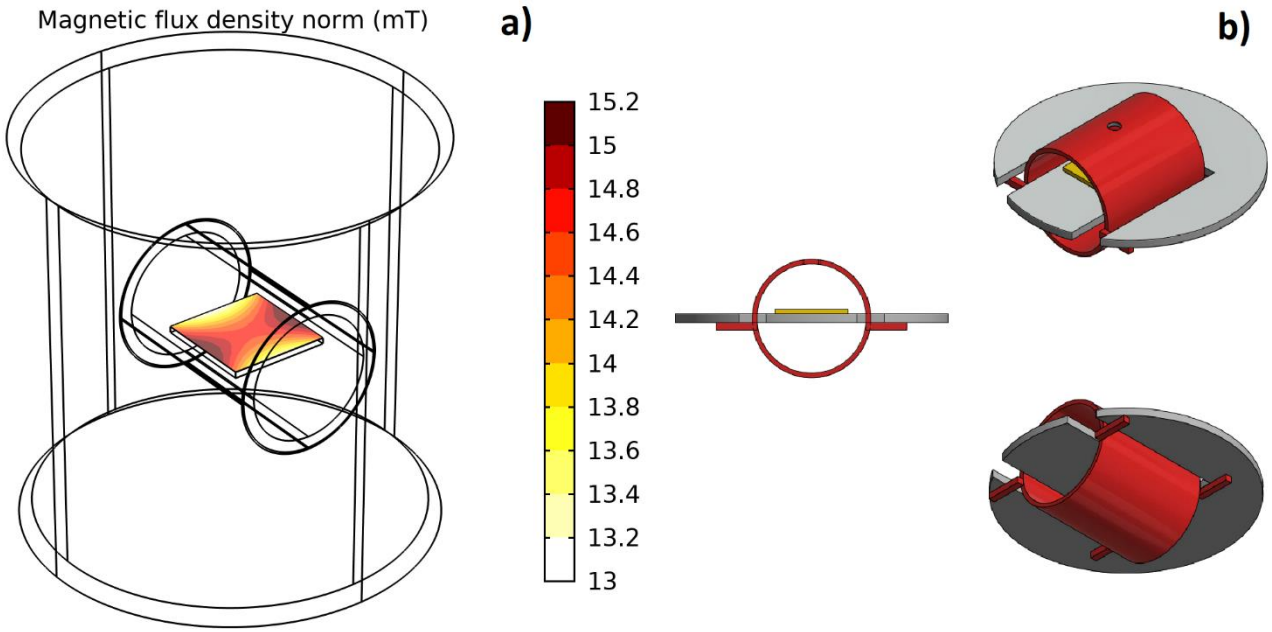

Figure 2.3. a) Simulation of magnetic field inside the coil. A uniform region is attainable with a field magnitude higher than 14 mT in the middle of the coil. Square region inside the coil is the detector chip. b) A schematic drawing of the coil geometry. The circuit board (grey) mounting the sample chip (yellow) has two gaps, where the coil(red) can be placed. The coil will be aligned and kept in place by small attachment pins at both ends (bottom right). The small hole at the top of the coil is needed for coupling in the X-rays. The resulting circuit board part from schematic b) will replace part 10 in Fig. 2.

The first field coil and modified sample stage to fit it has been built and tested and is ready for use in detector measurements. Calibration of its current vs field relationship will be performed with a commercial Hall sensor in the near future (sensor has been ordered).

This project has received funding from the European Union's Horizon 2020 research and innovation programme under grant agreement No 800923.

3. X-ray detector readout setup and characterization

To characterize and study the SuperTED as a calorimeter for X-ray applications, we have proposed to use a flux-transformer-coupled high-inductance SQUID current sensor as the readout system with our cryogenic apparatus. With the theoretical estimation and comparison that we have demonstrated in the previous report, as well as several discussions with SQUID experts and manufacturers, we have ordered a Magnicon C6XXL116 integrated two-stage SQUID chip and the associated XXF-1 FLL electronics as SQUID amplifier for the readout. However, due to the COVID19 related process problems and delays at the manufacturer facility (PTB Germany), the delivery time for the SQUID chip has been postponed (No date given). The room temperature FLL electronics were delivered in the summer of 2021.

To promote the assembly of the full readout setup and the cryogenic system, and to avoid further delay, we therefore mixed and matched our current sub-systems at hand by combining three elements from different sources: a substitutional commercial first-stage SQUID bare die device (Star Cryoelectronics), an existing second stage SQUID array, and the new FLL electronics from Magnicon. The new readout setup was designed as a temporary solution. When/if the more advanced Magnicon SQUID chip arrives, it can be substituted for the Star Cryo SQUID quickly. Currently, the readout system with the supporting cryogenics apparatus is assembled, tested and in use.

In the following section, we first very briefly explain the working principle of the SQUID and its readout. Then, we explain in detail both the planned readout scheme and the current implementation with the mix and match approach. In the end, we present the characterization results and quote the key metrics and performance of the current readout system.

3.1 Working principles

A dc SQUID is a device consisting of a superconducting loop interrupted by two Josephson junctions, each of which is connected with a parallel shunt resistor to eliminate hysteresis as illustrated in Figure 3.1(a). The sensing ability of the SQUID is based on two physical phenomena: flux quantization and Josephson tunneling.

This project has received funding from the European Union's Horizon 2020 research and innovation programme under grant agreement No 800923.

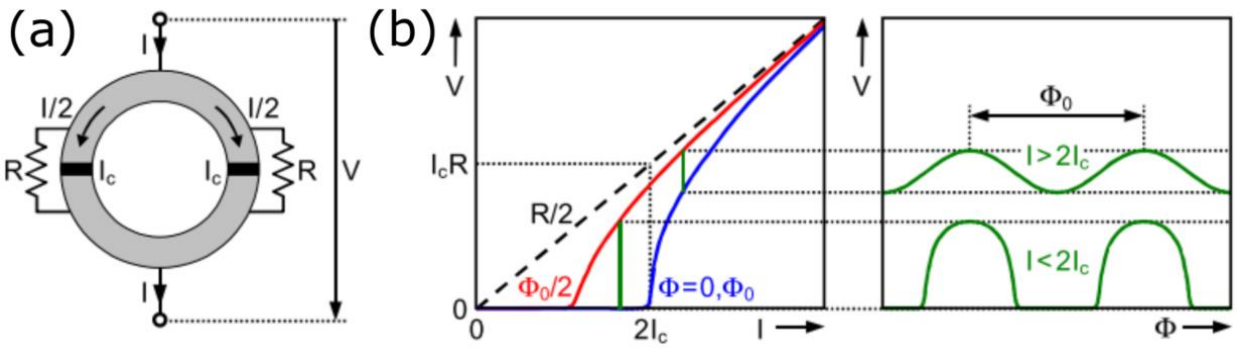

Figure 3.1. (a) Schematic of a SQUID circuit at zero applied magnetics flux. (b) I-V and V-φ characteristics of a SQUID. The dashed line shows the junction resistance without tunneling.

If a magnetic field is not present, a biased quasi-static current I will be split between the two junctions equally, and a voltage difference will develop across the device when $I/2$ is larger than the critical current I_c (neglecting the thermal rounding). When a magnetic flux is applied perpendicular to the SQUID loop, a circulating screening current I_s will be induced, leading to imbalanced currents $I/2 \pm I_s$ in the two junctions and an increased response voltage V. If the total external flux Φ in the loop exceeds half of the magnetic flux quantum ($\pm\Phi_0/2$ where $\Phi_0 = h/2e \approx 2.07 \times 10^{-15} Wb$), the quantized flux state of the SQUID will jump by Φ_0, the screening current I_s reverses its direction and begins to decrease the voltage upon further increasing of the magnetic flux, until the next flux state changes. In this way, as illustrated in Figure 3.1(b), a periodical relation between the loop flux Φ and the voltage V can be observed.

For a practical dc SQUID, the maximum voltage response δV to a small flux change $\delta\Phi$ in the loop occurs when $\Phi = (2n+1)\Phi_0/4$, which are the desired working points for the device. Within the linear regime of the oscillation $\Phi_{lin} \lesssim \Phi_0/\pi$, a maximum flux-to-voltage transfer coefficient $V_\Phi = |(\partial V/\partial\Phi)_I| = 2\pi R I_c/\Phi_0$ can be obtained based on resistively- and capacitively-shunted junction (RCSJ) model[9] for the Josephson junctions where R is the resistance of the shunt resistors. The noise performance of the SQUID at the working point can be evaluated from its noise energy per bandwidth $\varepsilon = S_\Phi/2L$, where S_Φ is the intrinsic flux noise density and L is the loop inductance.

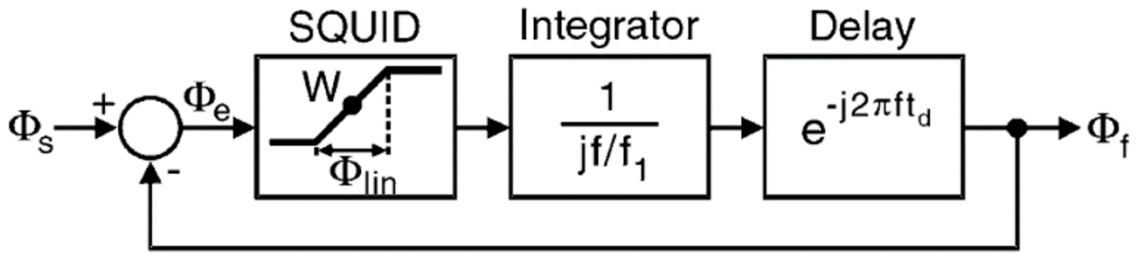

Figure 3.2. Simplified FLL transfer function model.

In order to keep the SQUID operating with the optimal linearized transfer function V_Φ , but for a much larger dynamic range while avoiding excess noise at large excursions from the working point, a flux-

This project has received funding from the European Union's Horizon 2020 research and innovation programme under grant agreement No 800923.

locked loop (FLL) scheme is commonly applied in a modern SQUID readout system. The dynamic behavior of the FLL can be understood as an ideal one-pole integrator with a delay element as shown in Figure 3.2. During the operation of the SQUID system, the signal flux Φ_s will be compensated with a feedback flux Φ_f, and as long as the error flux $\Phi_e = \Phi_s - \Phi_f$ remains within $\pm\Phi_{lin}/2$, the SQUID will behave as a linear device with a gain inversely proportional to frequency $G_{Int} = 1/(if/f_1)$ where f_1 is the unity-gain frequency of the open feedback loop. The system bandwidth and the stability of the feedback dynamics are limited by the effective delay t_d that approximates all the dynamic errors and phase shifts caused by the read-out electronics. For an optimized system, the unity-gain frequency, the maximum 3-dB bandwidth and the slew rate (feedback rise time) are expected to be $f_{1,max} = 0.08/t_d$, $f_{3-dB,max} = 0.18/t_d$ and $\dot{\Phi}_{f,max} = \Phi_{lin}/4t_d$.

As a conclusion to this section, we summarize the key metrics of the SQUID and the full readout system that will be characterized in the performance test. The intrinsic metric of a first-stage SQUID is the flux-to-voltage transfer coefficient V_Φ, which indicates the on-stage sensitivity of the readout in FLL mode. For the full readout system, the overall performance can be characterized by: (i) The gain from the signal input current to the output voltage of the readout. In FLL mode, this gain can be further broken down into the product of the feedback resistance (R_f) and a unitless gain factor; (ii) The slew rate ($\dot{\Phi}$) and 10% to 90% rise time, which are the key metrics to reflect how fast the readout can keep up with the signal pulse; (iii) The amplitude and the bandwidth of the current noise spectral density (S_I), which are the key metrices of the noise performance of the readout system and will have direct impact on the ultimate energy resolution of the measured detector.

3.2 Readout system

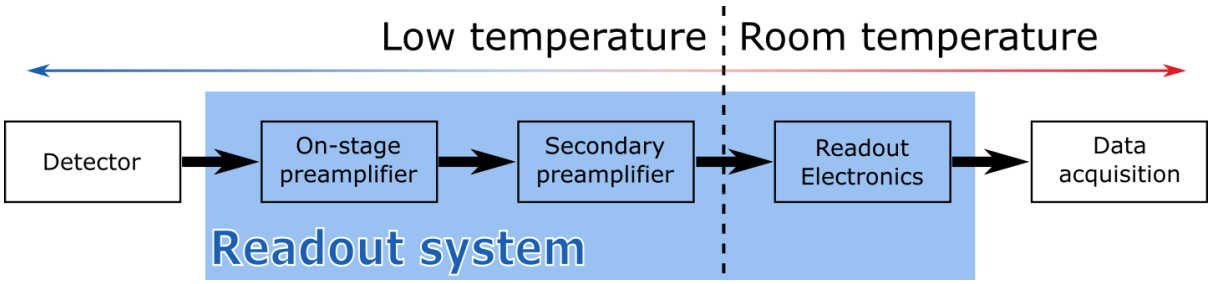

Figure 3.3. Simplified schematics of a readout system for low-temperature radiation detection.

A sensitive cryogenic readout system generally consists of three main stages: (1) an on-stage preamplifier, which is tasked to pick-up and amplify the small signal generated by the detector at the coldest stage, where the thermal noise is highly suppressed; (2) a secondary preamplifier that further amplifies the signal to match to the room temperature noise by the readout electronics; (3) the electronics that controls the I/O of the system, providing the command interface, biasing power for the amplifiers, operational parameter monitoring and the final output signal before the data acquisition.

This project has received funding from the European Union's Horizon 2020 research and innovation programme under grant agreement No 800923.

3.2.1 Planned readout setup

As demonstrated in the previous report D3.1, to meet the readout noise requirement of the SUPERTED detector [10], a flux transformer coupled SQUID with a large signal coil inductance is needed. The SQUID we plan to implement into the SUPERTED calorimeter readout system is an integrated two-stage C6XXL116 current sensor chip (C6) from Magnicon GmbH, which provides a transformer coupled integrated two-stage SQUID setup. In this setup both on-stage and secondary preamplifier are located on same chip and operated at the coldest temperature. The key specifications are briefly listed in Table 2.

Table 2: Key specifications of C6XXL116 SQUID

Signal coil inductance (L_S)	1.8 μH
Coupling factor (k)	0.72
Flux noise density ($\sqrt{S_\Phi}$)	0.25 $\mu\Phi_0/\sqrt{Hz}$ @ 0.3 K
Current noise density ($\sqrt{S_I}$)	~60 $fA/\sqrt{Hz}$ @ 0.3 K
Intrinsic noise energy (ε_{SQ})	~10 h @ 0.3 K
Chip dimension	$3 \times 3 \times 0.38\ mm^3$

Figure 3.4 illustrates the layout (a) and the basic circuit diagram (b) of the C6 SQUID chip. The small current signals generated by the detector will be fed into the input signal coil through a pair of aluminum superconducting bonding wires from the bounding pads +IN and -IN. The large input coil is wired as a first-order series gradiometer to reduce the sensitivity to homogeneous magnetic field [11]. An intermediate flux transformer with winding ratio of $40:1$ will match the input flux into the front-end SQUID. This first stage SQUID is based on Nb-AlOx-Nb trilayer superconducting tunnel junctions and realized as a second-order parallel gradiometer [12] with an effective loop inductance of $L_{SQ} \approx 80\ pH$. Besides the input signal flux, a feedback coil (+F/-F pads in Figure 6) is used for flux bias or flux lock, and an additional positive feedback (APF)[9] is used to distort the voltage-flux oscillation in order to enhance V_Φ. They are coupled into separate SQUID washers to minimize the coupling interference.

This project has received funding from the European Union's Horizon 2020 research and innovation programme under grant agreement No 800923.

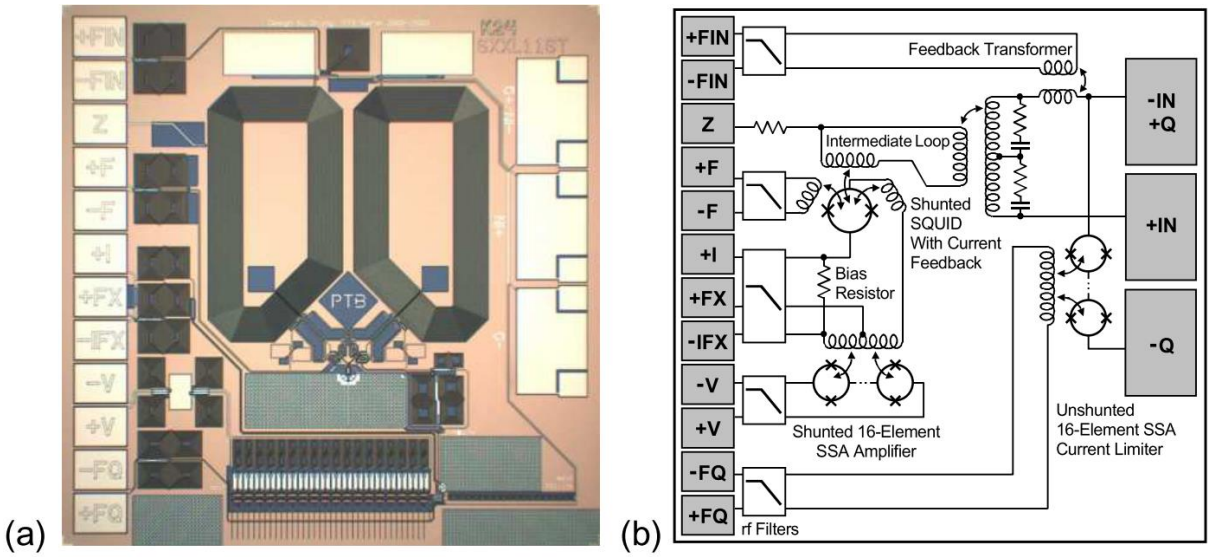

Figure 3.4. (a) Optical micrograph and (b) a simplified circuit illustration of the Magnicon C6XXL116 SQUID chip.

A second stage array of 16 identical low inductance ($\lesssim 3\ nH$) SQUIDs is inductively coupled to the front-end SQUID as an on-site preamplifier to further increase the total flux gain at the cold stage. As the signal-to-noise (SNR) ratio of the SQUID series array (SSA) scales up with the square root of the total number of SQUIDs, they are nearly ideal preamplifiers with a minimal impact on the overall noise performance of the sensor.[11] In addition, a single-SQUID-like overall flux-to-voltage characteristics of the two-stage SQUID can be obtained from the SSA amplified output by properly adjusting the bias flux through +FX, –IFX pads. The output signal is read through pads +V, -V.

This project has received funding from the European Union's Horizon 2020 research and innovation programme under grant agreement No 800923.

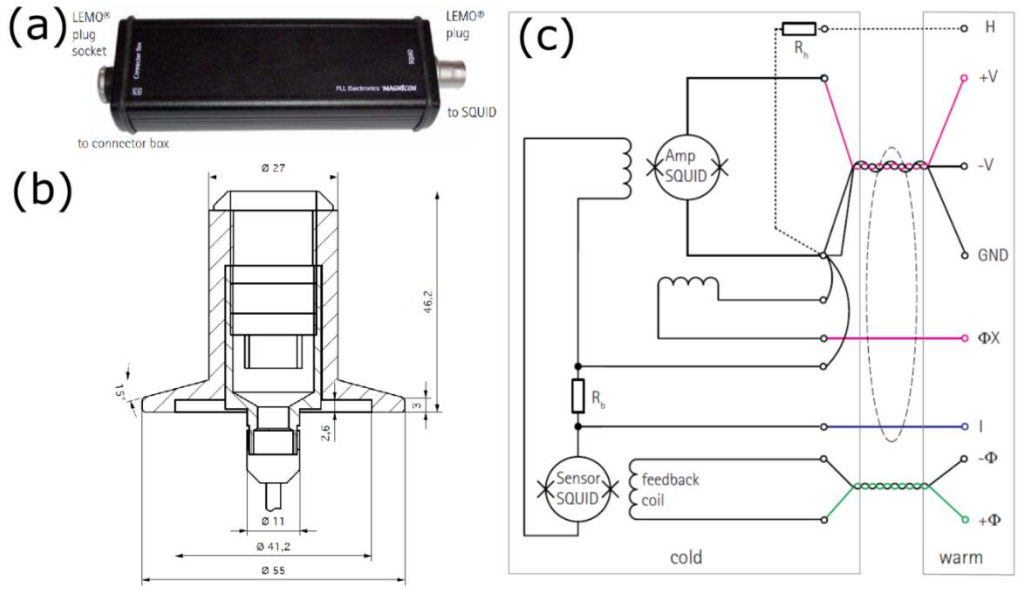

Figure 3.5. (a) XXF-1 flux-locked loop (FLL) electronics. (b) Vacuum tight 24pin LEMO socket integrated with DN40KF flange for direct FLL electronics mounting. (c) Connection scheme for C6XXL116 SQUID chip with XXF-1 electronics.

In order to significantly increase the stability and the dynamic range of the SQUID sensor to tolerate large interfering signals superimposed on the measurement signal, a flux-locked loop (FLL) scheme is preferred in the readout system. This technique is realized by a standalone XXF-1 FLL electronics (shown in Figure 3.5(a)) provided also by Magnicon GmbH.

All signals from and to the C6 SQUID chip are controlled and amplified by the FLL electronics through a 24 pin LEMO male connector (part #: FAG.3B.324.CLA). The female socket (part #: HGG.3B.324.CLLPV) of the LEMO connector is designed and integrated into a DN40KF flange with vacuum tight seals (shown in Figure 3.5(b)). In this way, the FLL electronics can be directly mounted on the cryostat without extra cable connections. In addition to improved protection from pick-up, the loop time between the SQUID and the feedback control is also minimized, leading to a lower delay time t_d and therefore a larger system bandwidth.

Inside the cryostat, seven wires for the signal connections are reserved between the LEMO socket at room temperature and the C6 SQUID chip at cold stage as illustrated in Figure 3.5(c). To minimize the noise and to improve the pre-amplifier common mode rejection, three twisted copper wires each with $< 5\ \Omega$ are used from room temperature to the 4 K stage for the $+V$, $-V$, and GND connections. The other signals (I, $\pm\Phi$, ΦX and heater H) are connected with ~ $50\ \Omega$ manganin wires to minimize the total thermal conductance from room temperature to 1.5 K. All wirings from room temperature are thermalized at 4K and 1.5 K stages in the cryostat, from which point on to the SQUID housing at the low-temperature end the connections are switched to NbTi superconducting wires, to further minimize the noise and thermal conductance of the wiring.

This project has received funding from the European Union's Horizon 2020 research and innovation programme under grant agreement No 800923.

The FLL electronics can be operated in two basic modes: an amplifier (AMP) mode and a normal FLL mode. In the AMP mode, the FLL electronics act as a faster amplifier with 3-dB bandwidth of 7 MHz, if the feedback resistor within the FLL electronics is disconnected from the feedback coil and the integration capacitor in the FLL electronics is shorted. This mode is mainly used for complete characterization of the SQUID and adjustment of its working point. The FLL mode is the common operation mode for the SUPERTED detector. Under this mode, the SQUID series array voltage between $\pm V$ connections is amplified, integrated and fed back into the feedback coil via $\pm \Phi$ connections. The differential preamplifier of the FLL electronics exhibits a first-order low-pass 3-dB bandwidth response at 0.3 MHz, whereas the integrator gain is made to compensate the preamplifier with a $1/f$ response below 0.3 MHz but frequency independent above the said frequency [13]. As the result, the overall integrator gain of the FLL is proportional to $1/f$ with a selectable gain-bandwidth product (GBP $= Gain \times \Delta f$) between 230 MHz to 7.2 GHz.

A separated connector box is used to connect the FLL electronics with laboratory computers during the operation. It distributes the signals, provides the system power, and utilizes an optically isolated RS-485 to RS-232 converter to isolate the readout electronics from the laboratory electromagnetic environment. The connector box and the related components (FLL cable, PC cable, analog output cables and power supply) are illustrated in Figure 3.6.

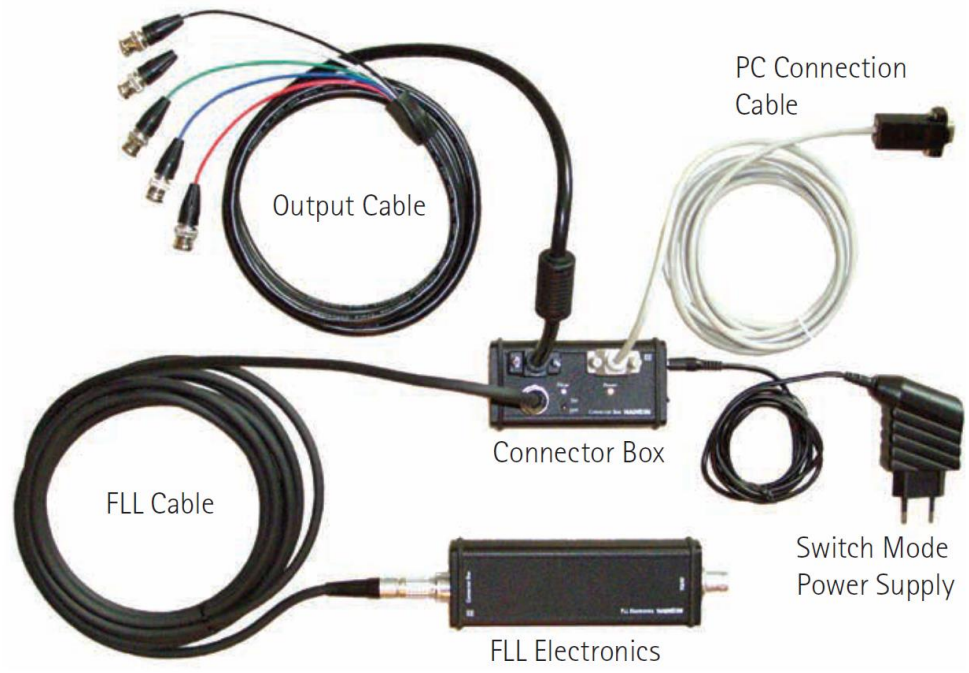

Figure 3.6. Hardware component of the readout electronics for Magnicon SQUID.

The connector box also includes a switchable second-order Bessel-type low pass anti-aliasing filter ($f_{3-dB} = 10\ kHz$), and a built-in signal generator which can be used to modulate all necessary signals with different selectable waveforms for possible sensor characterization and calibration.

This project has received funding from the European Union's Horizon 2020 research and innovation programme under grant agreement No 800923.

Analog signals can also be extracted from the connector box via VGA to 5-BNC connectors. The amplifier signals are output from the red, green and blue connectors, and the generator signal can be monitored via v-sync (black) line. The h-sync (white) cable can be used to apply additional external flux bias into the $\pm\Phi$ channels (feedback flux channel during SQUID operation).

The combined power consumption (including connector box, FLL electronics and the bias of SQUID) is about $1.8\,W$ with a $15\,V$ switch-mode power supply. Due to the optical isolation at the PC connection, a separated earth connection of the readout system will be established to the shield of the measurement room via analog output. In addition, a power pack with three $6\,V$ lead batteries are also viable as the system power supply for possible better noise performance.

3.2.2 Substitution setup

As mentioned previously, we have designed and implemented a substitutional setup to meet the milestone of the project, due to the delay of the Magnicon SQUID chip. After a survey on the current technology and on-shelf availability, we decide to integrate three key components from different sources into a mix-and-match readout system. The schematic diagram of the readout system is shown in Figure 3.7 (a) and a picture of the readout and cryostat in operation is shown in Figure 3.7 (b).

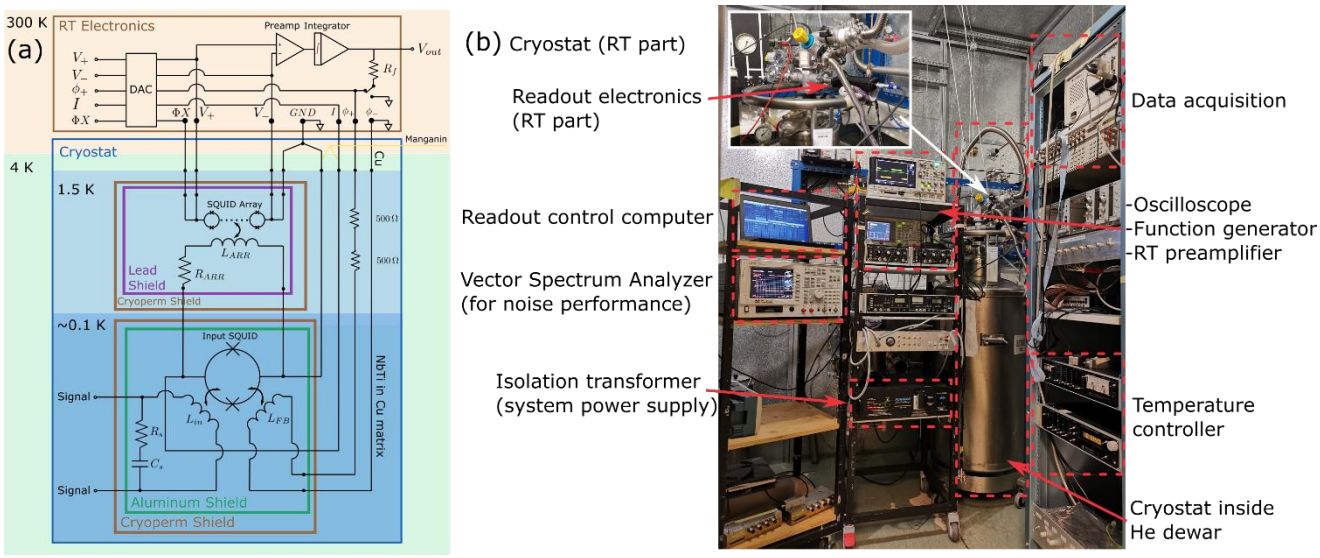

Figure 3.7. (a) Schematic of the electronic configuration of the implemented mix-and-match readout system. (b) Readout and cryogenic apparatus in operation.

The on-stage preamplifier used in this setup is a single SQUID chip (SQ2600) with an integrated large inductance flux transformer, provided by Star Cryoelectronics LLC. The key specifications of the SQUID are shown in Table 3. The SQUID die was wire bonded onto a removable stage (see Figure 3.8), which can be easily swapped with the Magnicon SQUID when it becomes available.

This project has received funding from the European Union's Horizon 2020 research and innovation programme under grant agreement No 800923.

Table 3: Key specifications of SQ2600 SQUID

Signal coil inductance (L_S)	$2.585\ \mu H$
Flux noise density ($\sqrt{S_\Phi}$)	$< 5\ \mu\Phi_0/\sqrt{Hz}$ @ $4.2\ K$
Current noise density ($\sqrt{S_I}$)	$< 0.5\ pA/\sqrt{Hz}$ @ $4.2\ K$
Intrinsic noise energy (ε_{SQ})	$\sim 160\ h$ @ $4.2\ K$
Chip dimension	$2 \times 3\ mm^2$

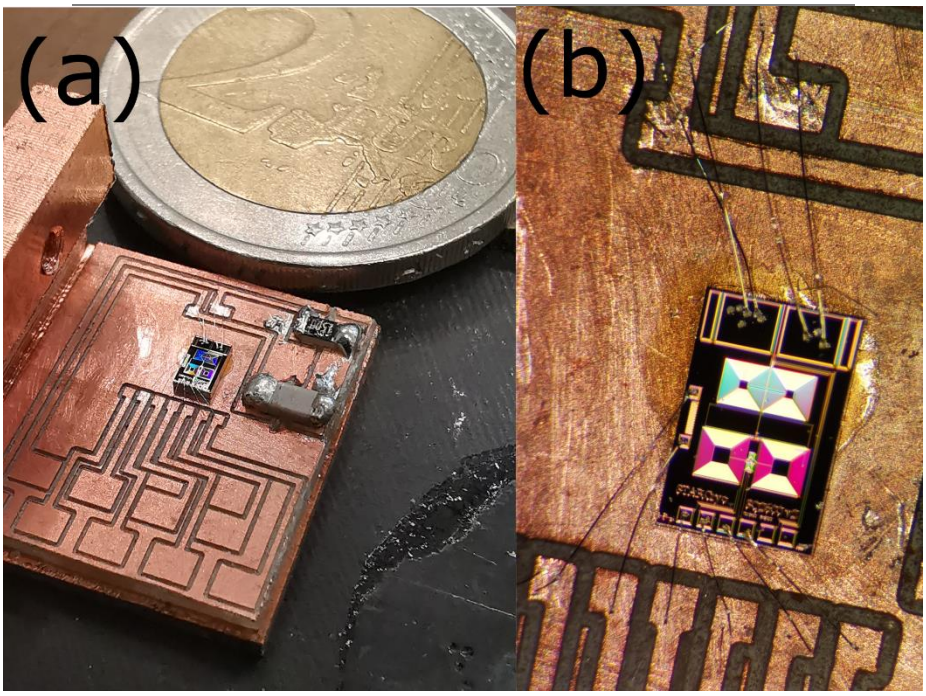

Figure 3.8. (a) Removable stage with wire bonded SQ2600 and RC shunt. (b) Zoom-in of SQ2600 chip with bonding wires.

An existing NIST SQUID array, which consists of 100 SQUIDs in series, is used as the second-stage preamplifier. The array is mounted on the higher temperature stage (1.5 K) for larger cooling power and housed inside a double-shielded tube-shaped container consisting of inner lead and outer Cryoperm casing. The SQ2600 signal will be inductively coupled to the array via lossless superconducting wiring and further amplified to match to the electronics noise at the room temperature. In addition, the array can be easily bypassed through additional wiring, allowing a quick swap to the Magnicon SQUID.

The Magnicon room temperature (RT) electronics and FLL electronics has been delivered to our site in August 2021 and have been integrated into the substitution setup as the final stage of the readout

This project has received funding from the European Union's Horizon 2020 research and innovation programme under grant agreement No 800923.

system. The wiring connections have been modified to adapt to the new SQUID configuration as shown in Figure 3.7 (a).

3.3 Readout characterization and performance test

In this section, we will use the superconducting flux quantum $\phi_0 \approx 2.07 \times 10^{-15} Wb$ as a general unit. It can easily be converted to current units with the help of readout specific parameters such as the feedback mutual inductance ($1/M_{Fb} = 11.59\ \mu A/\phi_0$) or signal input mutual inductance ($1/M_{in} \approx 0.1\ \mu A/\phi_0$).

The characterizations of the SQ2600 SQUID (without the secondary amplification) are presented in Figure 3.9. The I-V characteristic of the SQUID has been used to extract the dynamic conductance for different current bias values (see Figure 3.9 (a) and inset), which helped the optimization of the bias resistor of the SQUID. The V-Φ modulations under different current biases have been plotted in Figure 3.9 (b). The peak-to-peak value V_{pp} (blue dots in Figure 3.9 (c)) and the transfer function V_Φ at the largest slope (red dots in Figure 3.9 (c)) of the modulations have been extracted as a function of the current bias. As a reference, the specification provided by Star Cryoelectronics guarantees $V_{pp} \geq 30\ \mu V$ and $V_\Phi \geq 200\ \mu V/\phi_0$. Those specifications were surpassed for bias currents below ~25 µA.

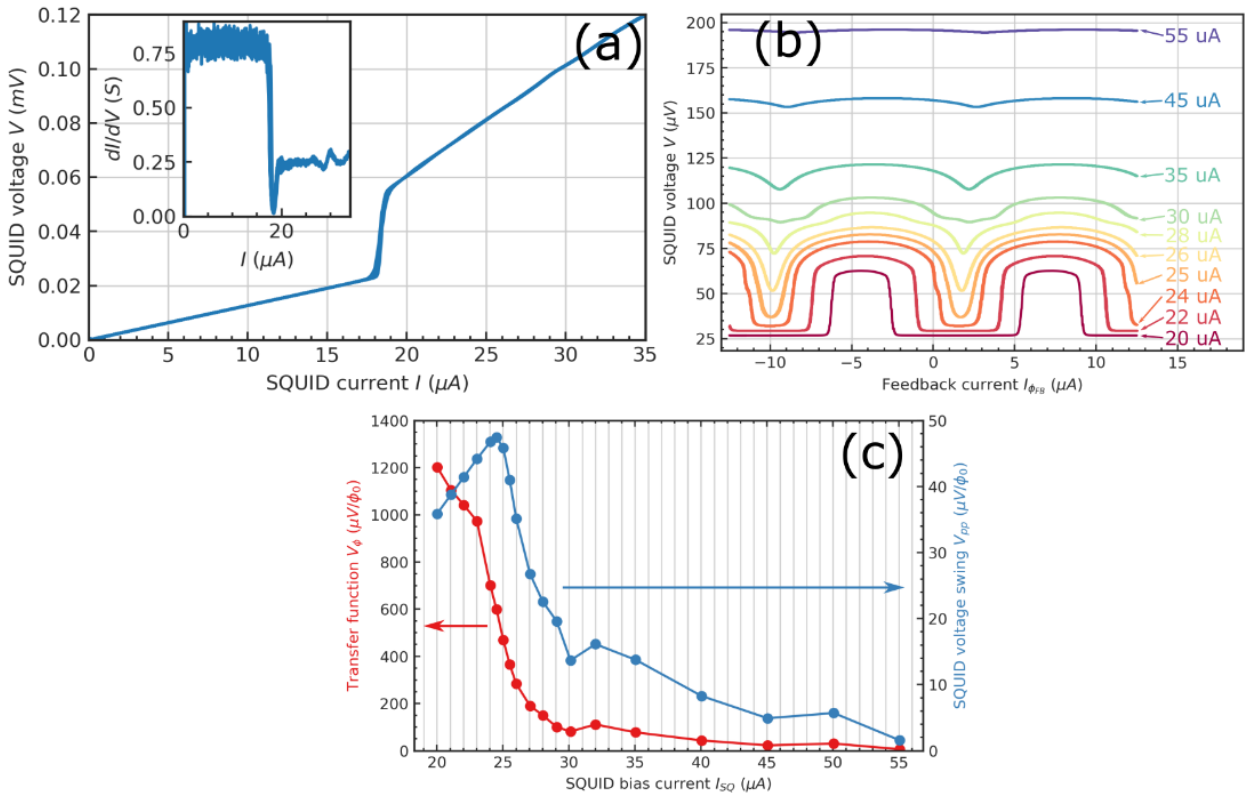

Figure 3.9. (a) I-V characterization of SQ2600 SQUID, the inset shows the dynamic conductance of SQUID as a function of the current bias. (b) $V - \Phi$ modulation of SQ2600 SQUID at different current

This project has received funding from the European Union's Horizon 2020 research and innovation programme under grant agreement No 800923.

bias points. (c) SQ2600 flux-to-voltage transfer function V_ϕ and peak-to-peak voltage swing V_{pp} under different current bias values. Measurements were performed at 1.5 K.

The combined V-Φ modulations of both the first- and the second-stage SQUIDs are presented in Figure 3.10. The plots in (a) and (b) are the overall modulations of the full readout under different first-stage SQUID biases and array biases, respectively. It can be seen that the combined modulation of the readout behaves similar to a single-SQUID modulation, indicating a good matching between two SQUID amplifiers. In addition, this also allows us to operate and adjust the readout SQUID as if it is a single SQUID. In Figure 3.10 (c), we plot several modulations with fitted transfer functions V_ϕ (illustrated as dashed lines) from different measurement runs. In run240 (red curve), only the first-stage SQUID was measured. Several optimizations and improvements were carried out on both readout and cryostat from run242 to run245, and we have achieved an overall transfer function $V_\phi = 19\ mV/\phi_0$ in the current substitutional setup, about 50-fold increase over the single SQUID result.

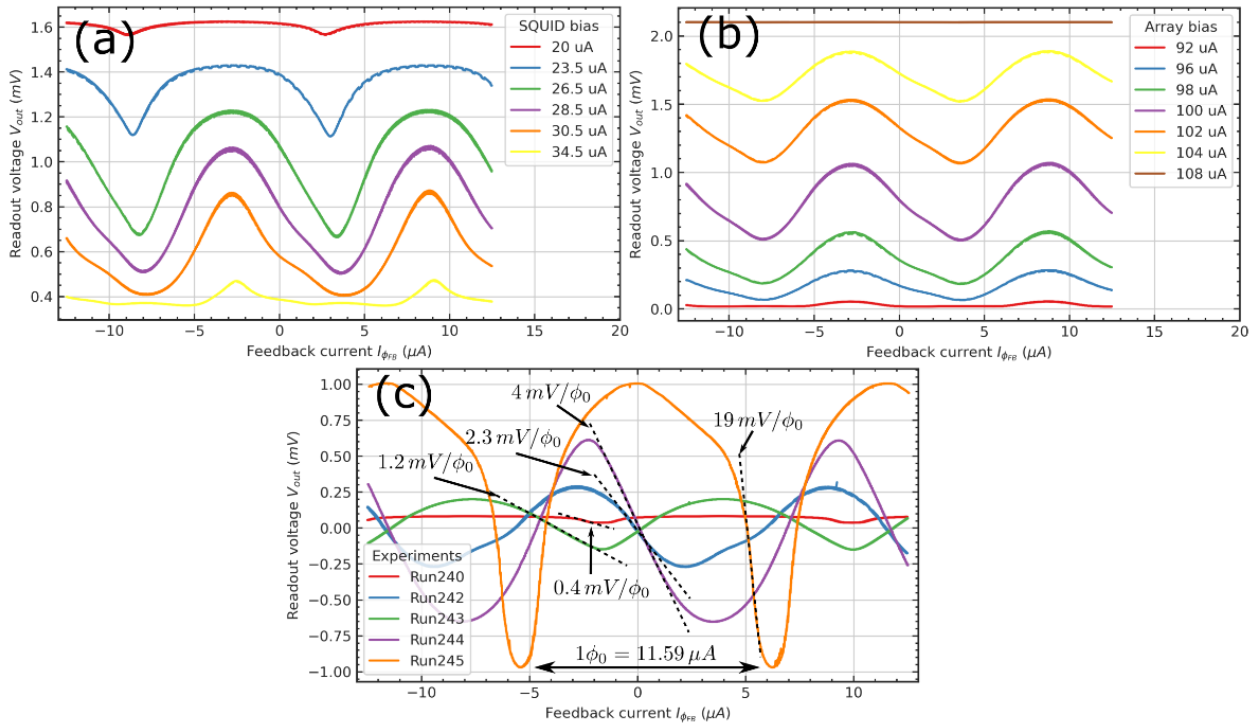

Figure 3.10. (a) Combined V-Φ modulation under different first SQUID bias. Array bias was set to 100 μA. (b) Combined V-Φ modulation under different array bias. First stage SQUID bias was set to 26.5 μA. (c) V-Φ modulation comparison. Run240 measured only the first-stage SQUID. Several optimizations and improvements have been done from Run242 to Run245 to increase the performance of the readout. Run240 was performed at 1.5 K, Run242 was performed at <200 mK, Run243 was performed at 600 mK, Run244 was performed at 0.5 K, and Run245 was performed at <300 mK.

The gain of the SQUID readout system is a key metric, which can be defined as the ratio between the output voltage to the input current signal ($Gain = V_{out}/I_{in}$) with a unit of resistance. Under the FLL

This project has received funding from the European Union's Horizon 2020 research and innovation programme under grant agreement No 800923.

mode, readout gain can be calibrated using $Gain = R_f \times Gain\ factor$, in which R_f is a known and adjustable feedback resistance in the feedback loop, whereas the gain factor is an intrinsic device parameter that is determined by the signal coil and feed back coil mutual inductances and can be calibrated. In the left plot in Figure 3.11, we present the low-frequency calibration results with different R_f values and operation temperatures. The readout output voltage was measured as a function of a clean, slow-sweeping current signal in the input that was generated from a floated battery source (see inset plot). The calibrated value is about $120\ V/V$, and is consistent under different operation parameters. Based on the choice of R_f, the gain of the readout can be extracted, *e.g.* with $R_f = 100\ k\Omega$, the gain is $1.2 \times 10^7\ V/A$. In the right plot, we present an alternative calibration method by measuring the output response against a square wave generated by a function generator.

We should note here that in the above measurement of the dynamic response of the readout, the signal input was connected from the coldest stage directly to room temperature (RT) without filtering. This allowed the RT noise (thermal, grounding, environment, power supply, *etc.*) to be fed into the readout, leading to bandwidth, noise performance and stability degradation. However, the consistency of the gain factor measurements demonstrate the robustness of the current readout system. In the future TED experiments, the signal will be generated at the coldest stage locally and maximized performance can be expected.

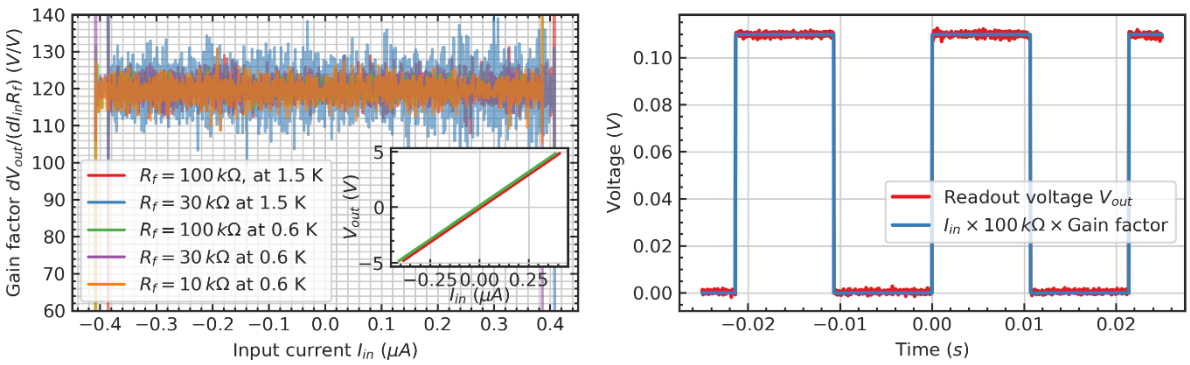

Figure 3.11. (Left) Low-frequency calibration of the readout gain factor with different operation parameters (R_f and temperature). The inset shows the raw calibration data, in which the output voltage was measure against a slowly sweeping input current in FLL mode. (Right) An alternative low-frequency calibration using a current square wave as input, with measurement of the output voltage response.

The signal pulse generated by the X-ray calorimeter can be very fast. A high-resolution TES can have a characteristic decay time as fast as tens of microseconds [17]. To keep up with the pulse signal and preserve the fidelity of the pulse shape, the response speed of the readout system is a key metric. The slew rate and the 10%-90% signal rise time have been widely used to describe the small and large signal response speed of SQUID readouts in time domain. In Figure 3.12 (a), we present the measured slew rate and rise time of the readout. Two different Gain-Bandwidth Products (GBP) are

This project has received funding from the European Union's Horizon 2020 research and innovation programme under grant agreement No 800923.

demonstrated (orange and blue curve) in the plot. GBP is an adjustable parameter of the RT electronics, and a higher GBP setting leads to a faster slew rate and rise time, if the system gains are identical. The green curve in Figure 3.12 shows the readout response with better optimized transfer function. The working point was carefully chosen 1) to avoid distortion in the V-phi modulation curves, and 2) to avoid the clipping of the modulation at the peak and the valley, 3) while maximizing the transfer function slope at the working point. With a higher intrinsic gain, the performance of the slew rate and the rise time are enhanced under the same GBP. In plot (b) and (c), the responses of the readout to faster square pulses are demonstrated. The readout with the lower GBP can correctly represent a 10 μs square pulse (50 kHz, 50% duty cycle), but lost 25% of the peak height for a 2.5 μs pulse (200 kHz, 50% duty cycle). On the other hand, under the optimized operational settings with 4 GHz GBP, the faster pulse response was correctly obtained. We should emphasize again that due to the presence of the RT noise in these measurements, the performance of the readout with an actual TED can be expected to be faster owning to the enhancement in both the transfer function and the system bandwidth. From these measurements, the best rise time is 0.8 μs and the slew rate is 0.12 $\phi_0/\mu s$, however based on the estimated loop delay time $t_d \approx 200\, ns$ of our current setup, we can expect 0.4 $\phi_0/\mu s$ as the maximum slew rate without the presence of RT noise.

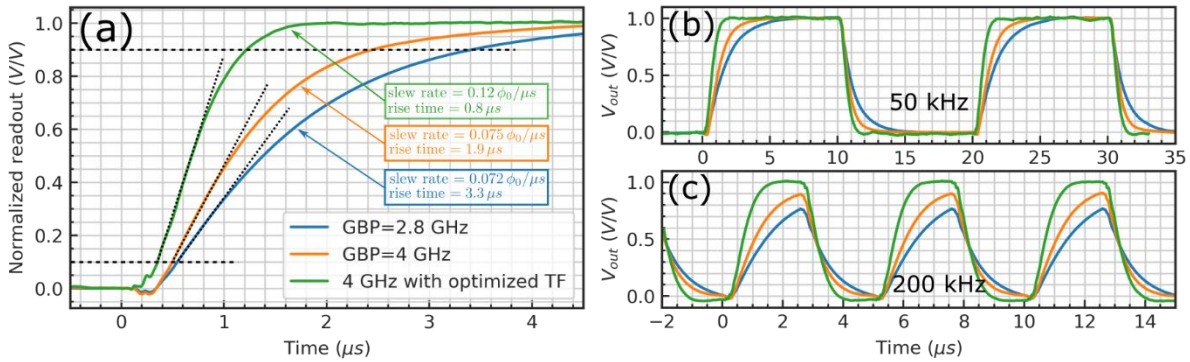

Figure 3.12. (a) Transient responses of the readout voltage to step-up input current. (b) and (c) Normalized readout voltage responses to 50 kHz and 200 kHz input square waves (50% duty cycle).

Lastly, we present the noise performance of the readout system. The noise spectral density and the noise bandwidth are key metrics that can have a significantly impact on the energy resolution of microcalorimeter. The noise we present in Figure 3.13 were converted into an input equivalent current noise using the calibrated gain of the readout.

This project has received funding from the European Union's Horizon 2020 research and innovation programme under grant agreement No 800923.

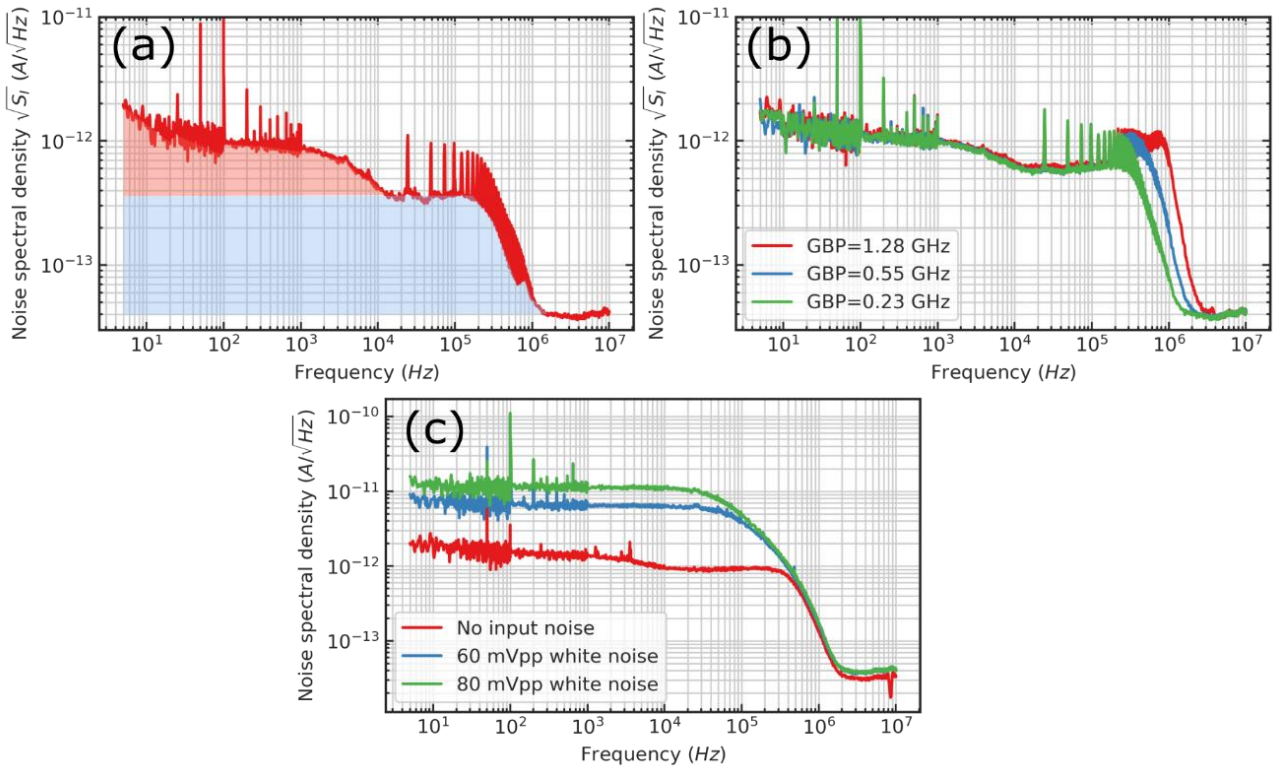

Figure 3.13. (a) Input equivalent readout current noise in the quiescent state. The unit is in current amplitude spectral density $A/\sqrt{Hz}$. (b) Equivalent current noise bandwidth under different GBP. (c) Readout frequency response, where the readout equivalent current noise was measured for different input white noise levels.

In plot (a) we demonstrate the current noise at 300 mK with the RT input wirings disconnected. Two noise plateaus (roll-offs) were observed. We believe the plateau at $\sqrt{S_I} \approx 0.3\ pA/\sqrt{Hz}$ in the frequency range between $10\ kHz$ to $200\ kHz$ is the noise level dominated by the intrinsic noise of the first-stage SQUID, given their advertised noise specification is $< 0.5\ pA/\sqrt{Hz}$. The source of the second $\sim 1\ pA/\sqrt{Hz}$ plateau at frequencies $< 1\ kHz$ is unknown. However, the increased noise level at low frequency has a small effect on the microcalorimeter energy resolution. This is because it is the total noise power, which is the integration of S_I over the full bandwidth, that will determine the optimal filter to estimate the energy resolution [18]. The noise power contribution of the red area in plot (a) is less than 3% of the total noise power. In addition, resonance and harmonic peaks were observed beginning from $25\ kHz$ in plot (a). These noise peaks were identified as clipping noise of the RT amplifier caused by the overloading in the electronics. This problem was adjusted and removed in the later experiments, see *e.g.* the red curve in Figure 3.13 (c).

The noise bandwidth of the readout is demonstrated in Figure 3.13 (b). By increasing GBP, the system bandwidth can be increased up to $800\ kHz$. We think this is limited by the loop delay of the full readout chain and the estimated the delay is about $t_d \approx 200\ ns$.

This project has received funding from the European Union's Horizon 2020 research and innovation programme under grant agreement No 800923.

In Figure 3.13 (c), experiments are shown where white noise was directly fed into the signal input, and the readout noise spectrum was then measured. Flat noise levels have been shown across the full available bandwidth, indicating a uniform frequency response of the readout system. In addition, this also proved that the previously observed roll-off of the noise level in the frequency range between 1 kHz to 10 kHz was not caused by an unwanted attenuation of the input signal.

3.4 Conclusion

We have reported the successful installation status of the X-ray SQUID readout system. Although the delivery of the planned SQUID sensor was delayed due to the pandemic, we were able to design, build and test a substitution system to delivered to the consortium in a relatively short period of time. We reported a comprehensive study of the characteristics of the current setup with key metrics and performance figures. The readout system and its associated cryogenic apparatus are now prepared in a ready-to-use state. In addition, the current substitutional system was designed and built in a way that is fully compatible with the planned installation of the more advanced SQUID sensor, which can be easily and quickly implemented to further improve the performance of the readout.

4. Near future practical steps on the setup

- We have notified the radiation safety manager of the X-ray source on our preliminary plan. The dimensions of the source have been identified. We will prepare the necessary plans and documents for transportation and implementation of the source.
- With the provided dimension information, the implementations of the X-ray source and collimator are discussed and under design.
- The next version of the magnetic coil that is compatible with the X-ray source will be assembled (NbTi wire+support) and made ready for the sample stage, after the scheme for x-ray source collimation and alignment design is finalized.

This project has received funding from the European Union's Horizon 2020 research and innovation programme under grant agreement No 800923.

5. iKID (alternative) readout development: basic principles, design and first prototype

This 'iKID *read-out implementation*' presents the principle, the current status (design, prototype, test) and the perspectives of a read-out implementation for thermoelectric detectors using LC-resonators made out of a superconductor thin film. The current generated by the thermoelectric detectors is to be circulated into a resonator. The current is then detected through a change of the resonance frequency of the resonator. The advantage of this approach lies in the large multiplexing factor that is potentially achievable, and the use of existing KID readout electronics and already wired cryostat in CNRS. On the other hand, optimally the readout can be this way decoupled from the point of signal detection, maintaining the benefits of biasless thermoelectric detection.

5.1 Basic principles

The thermoelectric detectors TED are expected to generate a current when absorbing electromagnetic radiation. For typical millimeter detection applications, the incoming power per detector can be considered to be roughly of the order of 1 pW, resulting in an output current of the order of 800 pA for a detection efficiency of 50%. In order to achieve a desired sensitivity of 0.1fW/Hz$^{0.5}$, the readout system should be able to guarantee a noise better than 0.1 pA/Hz$^{0.5}$.

For the iKID read-out implementation, current detection will be realized by monitoring variations of the resonance frequency of kinetic inductance detectors. The current generated by the thermoelectric detectors will be sent into a Kinetic Inductance Detector. In turn, the resonance frequency of the KID will vary with the current. For a current I small compared to the critical current I^* the frequency shift is expressed as follow:

$$[f(I)-f(0)] / f(0) \sim - \alpha/2 \, (I/I^*)2 \qquad (1)$$

where $\alpha = Lk/(Lk+Lg)$ is the ratio of the kinetic inductance by the total inductance (kinetic plus geometric).

A. Kher and collaborators [14] have demonstrated a current sensitivity of 8 pA/Hz$^{0.5}$ for a resonator made of 10-nm-thick sputtered TiN on Si. Fig. 5.1 shows the shift observed for an injected current of ~60 μA.

This project has received funding from the European Union's Horizon 2020 research and innovation programme under grant agreement No 800923.

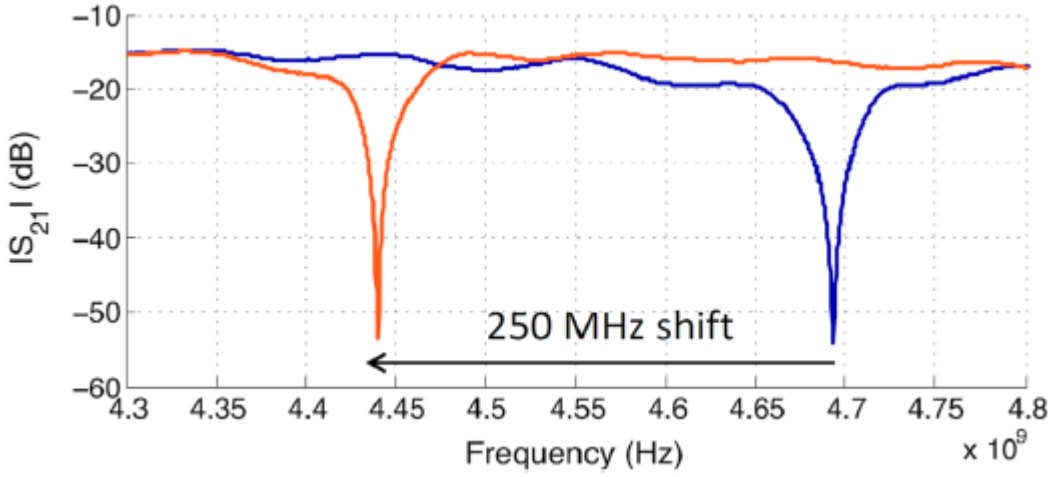

Figure 5.1. Shift of the resonance frequency for an injected dc-current of ~60 μA (from A. Kher et al., [14]).

To detect a small current, equation (1) shows that a small critical current I* is needed. For this purpose, two parameters can be optimized: the critical current density J* , that is material dependent and the smaller cross-section S of the kinetic inductance design as I*=J*S. In disordered superconductor materials, small critical current density can be achieved, like in granular aluminum, for which J* ~ $3x10^{10}$ Am^{-2} [15,16]. Using electron-beam lithography, widths as small as 100 nm can be obtained for a superconducting film thickness of the order of 50 nm. Eventually, we estimate that for superconducting granular aluminum (that we are familiar with), it is possible to achieve critical current as low as 150μA. For a resonance at 1 GHz such critical current leads to a frequency shift of 320 MHz for an injected current of 60 μA and to a frequency shift of 14 kHz for an injected current of 800 pA. Thus, in principle, such a read-out scheme could detect the 800 pA generated by the thermoelectric detectors TED for typical millimeter detection application.

In collaboration with KIT (Karlsruhe Institute of Technology, I. Pop, P. Paluch) we have designed, realized and tested a first prototype.

5.2 Design

We have performed extensive electromagnetic radio-frequency simulations using the SONNET software to optimize a design. The input parameters are the dielectric properties of the materials (substrate and superconductors) and the design of the structure. **The general problem is to design a resonator that achieves a high quality factor even though it is connected to detectors with small impedances (less than one Ohm).** To achieve this, we use two different granular aluminum (grAl) compositions: a “low” kinetic inductance grAl for the resonator part (marked in red in Fig. 5.2) and a “high” kinetic inductance grAl for the two lines connecting the resonator to the detector (green in fig. 5.2). The lines act as a low-pass filter: it allows the dc-current to flow from the detector to the

This project has received funding from the European Union’s Horizon 2020 research and innovation programme under grant agreement No 800923.

resonator, but prevents the resonating ac-current to leak out the resonator, ensuring a high resonator internal quality factor.

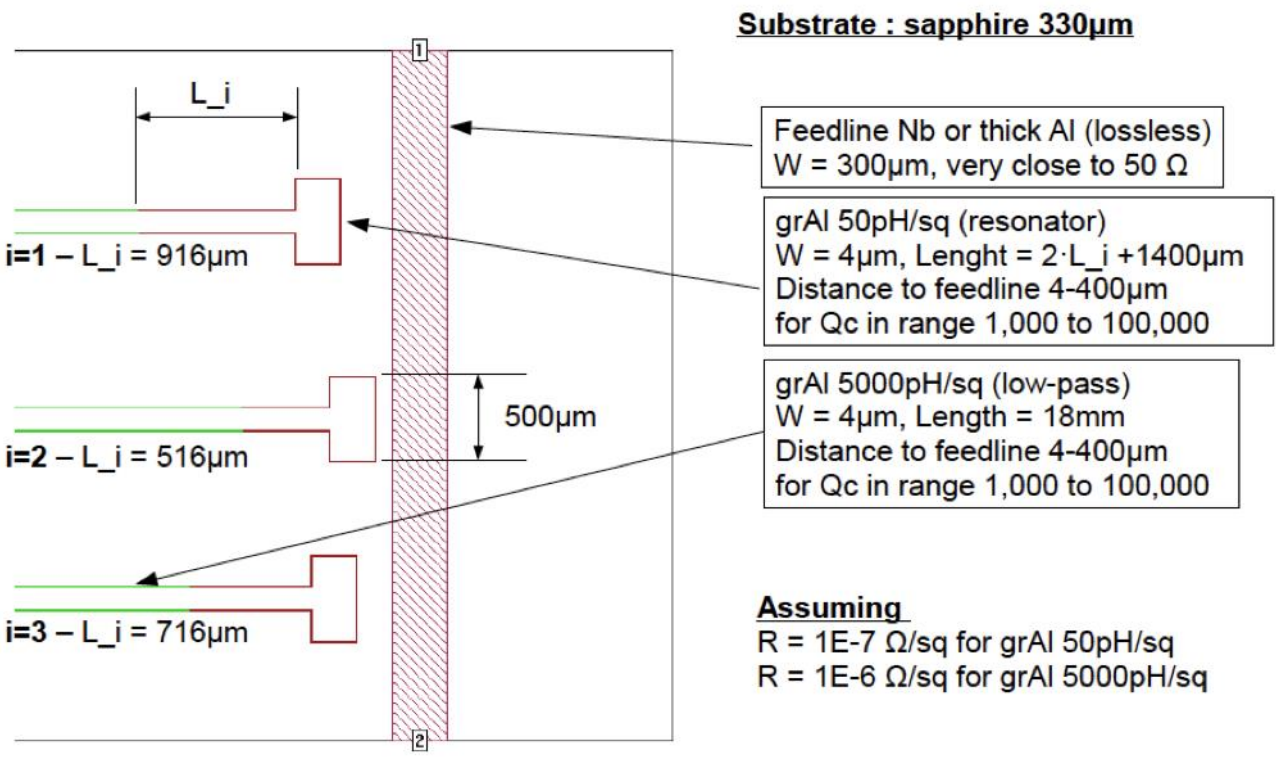

Figure 5.2. Zoom on the design of the iKID readout scheme. Resonators (in red) are to connect to the detectors (not shown) via the dc-current lines (in green). The red vertical line is a RF- feedline to monitor the resonance frequencies of the Kinetic Inductance Detectors.

Fig. 5.3 shows some of the electromagnetic radio-frequency simulation results. The main panel displays the magnitude of the transmission coefficient of the feedline: the three dips correspond to the three resonances (5.3 GHz, 5.7 GHz and 6.0 GHz). The three insets present the current distribution for each resonance frequency: red and blue correspond respectively to high and low current density. The quality factor of each resonance is suitable for detection and the resonance distribution over one GHz at about 6 GHz is easy to span with the electronics.

This project has received funding from the European Union's Horizon 2020 research and innovation programme under grant agreement No 800923.

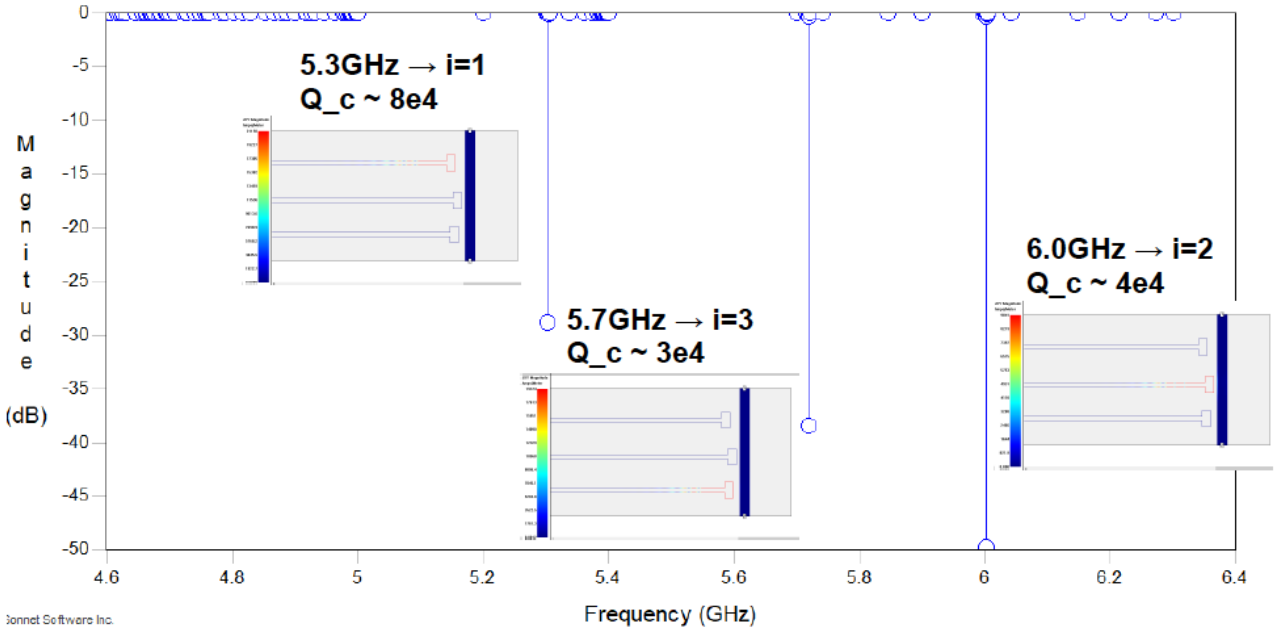

Figure 5.3. electromagnetic radio-frequency simulation results. Main panel: magnitude of the transmission coefficient of the feedline versus frequency. Three high quality factor resonances are visible. Insets: current distribution for each resonance frequency. High current in red, low current in blue.

Eventually, the design optimized with the electromagnetic radio-frequency simulation is presented in Fig. 5.4. For test purposes, thirteen resonators are designed but only eight are connected to dc-current ports (resonators #6 to #13). For this design the minimum width of the resonator line is 4 μm**.**

This project has received funding from the European Union's Horizon 2020 research and innovation programme under grant agreement No 800923.

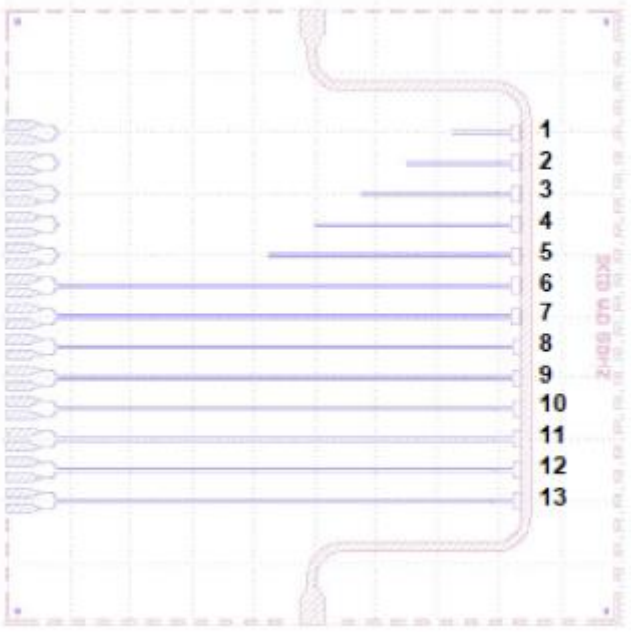

Figure 5.4. design of the iKID readout scheme. Thirteen resonators are designed. For test purposes, only eight are connected to dc-current ports (resonators #6 to #13). The vertical red line is the RF-feedline to monitor the resonance frequencies of the resonators.

5.3 Prototype

The prototype iKID chip was realized by our collaborators, I. Pop and P. Paluch from Karlsruhe Institute of Technology (KIT), Germany. Fig. 5.5 shows the prototype inserted in a specially designed (by CNRS) sample holder with an ad-hoc PCB-board. The PCB-board (at the bottom) is connected on one side to the resonators via micro-bonding and on the other side to cables. The cables allow sending a dc-current from room temperature sources to the resonators.

This project has received funding from the European Union's Horizon 2020 research and innovation programme under grant agreement No 800923.

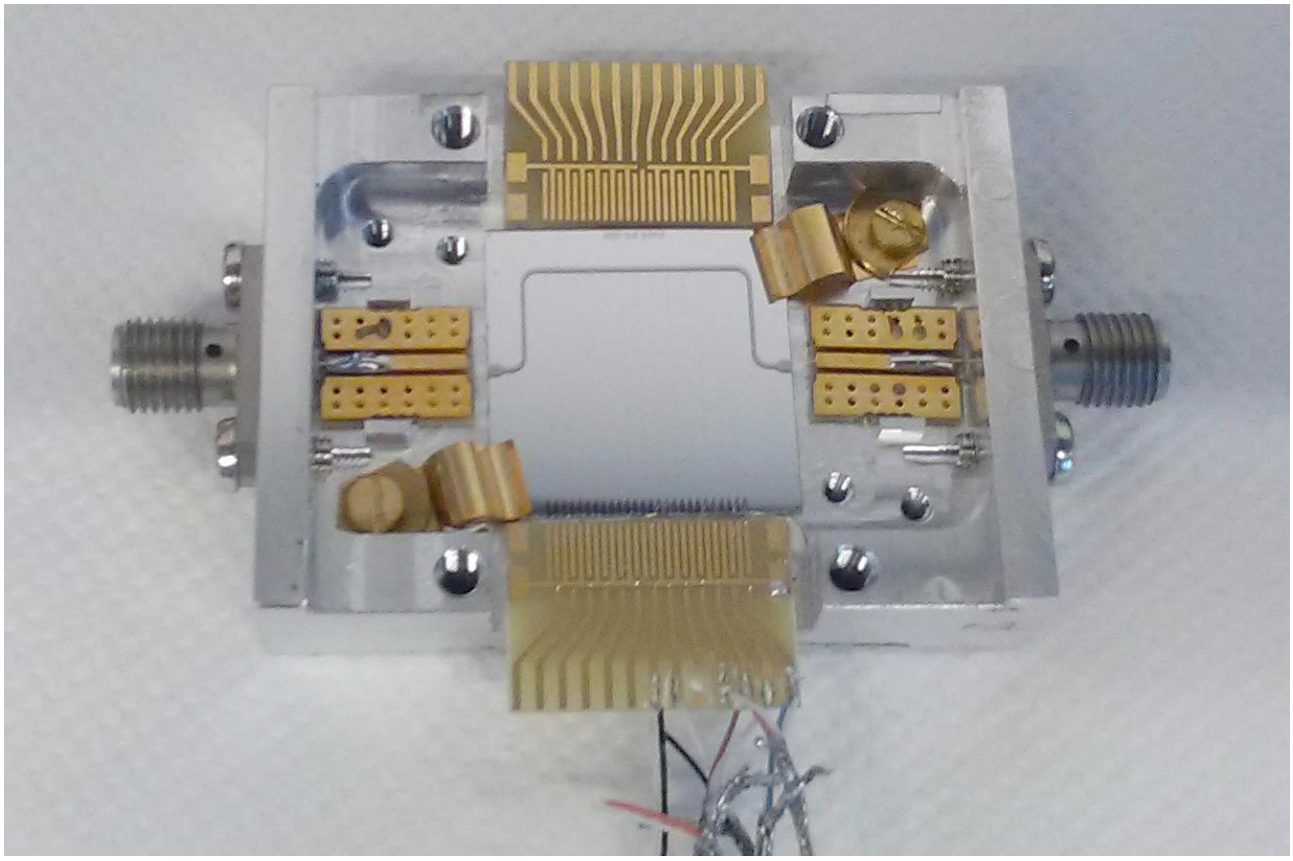

Figure 5.5. photo of the first prototype of the iKID readout scheme. The matrix of thirteen resonators is in the center. Only the feedline is clearly visible: it is the horizontal line. The bottom PCB-board is connected to the resonators and to cables.

The resistances of the different layers were measured on test sets: Figure 5.6 presents the results. The actual kinetic inductance of the resonator part (2) is close to the target value of 50pH/sq but the kinetic inductance of the line part (3) is small compared to the target value of 5nH/sq. Besides, the measured contact resistance between the two granular aluminum layers were ranging from 30 kΩ up to immeasurable value.

This project has received funding from the European Union's Horizon 2020 research and innovation programme under grant agreement No 800923.

1. 15 nm Nb
    - R~70 Ω/sq
    - L~10pH/sq
2. 50 nm grAl
    - R~120 Ω/sq
    - L~75pH/sq
3. 25 nm grAl
    - R~2.3 kΩ/sq
    - L~1.5nH/sq

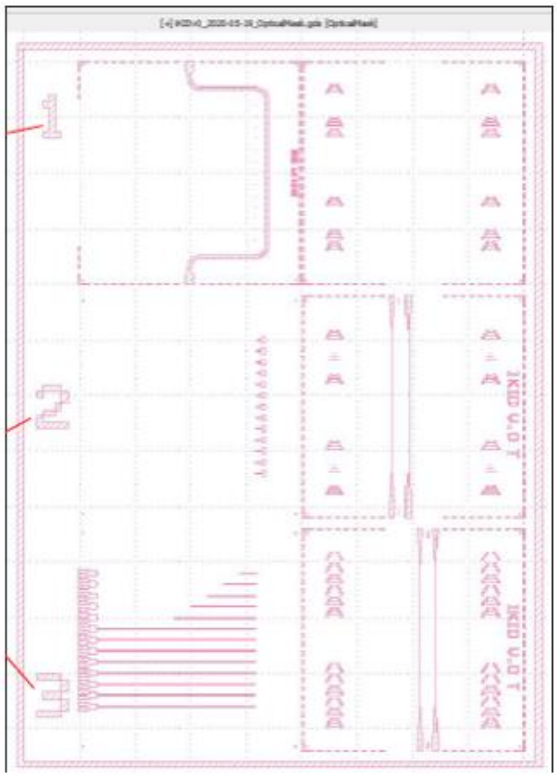

Figure 5.6. Resistance and inductance of the different layers of the iKID prototype.

5.3 iKID testing

The prototype was cooled down at 100 mK, in one of the CNRS dilution refrigerators used for the SUPERTED project, with three resonators connected to a device allowing to send three different values of dc-current ranging from 10 pA to 1 mA and to measure in a four point configuration the resistance of the resonators (R1, R2 and R3).

This project has received funding from the European Union's Horizon 2020 research and innovation programme under grant agreement No 800923.

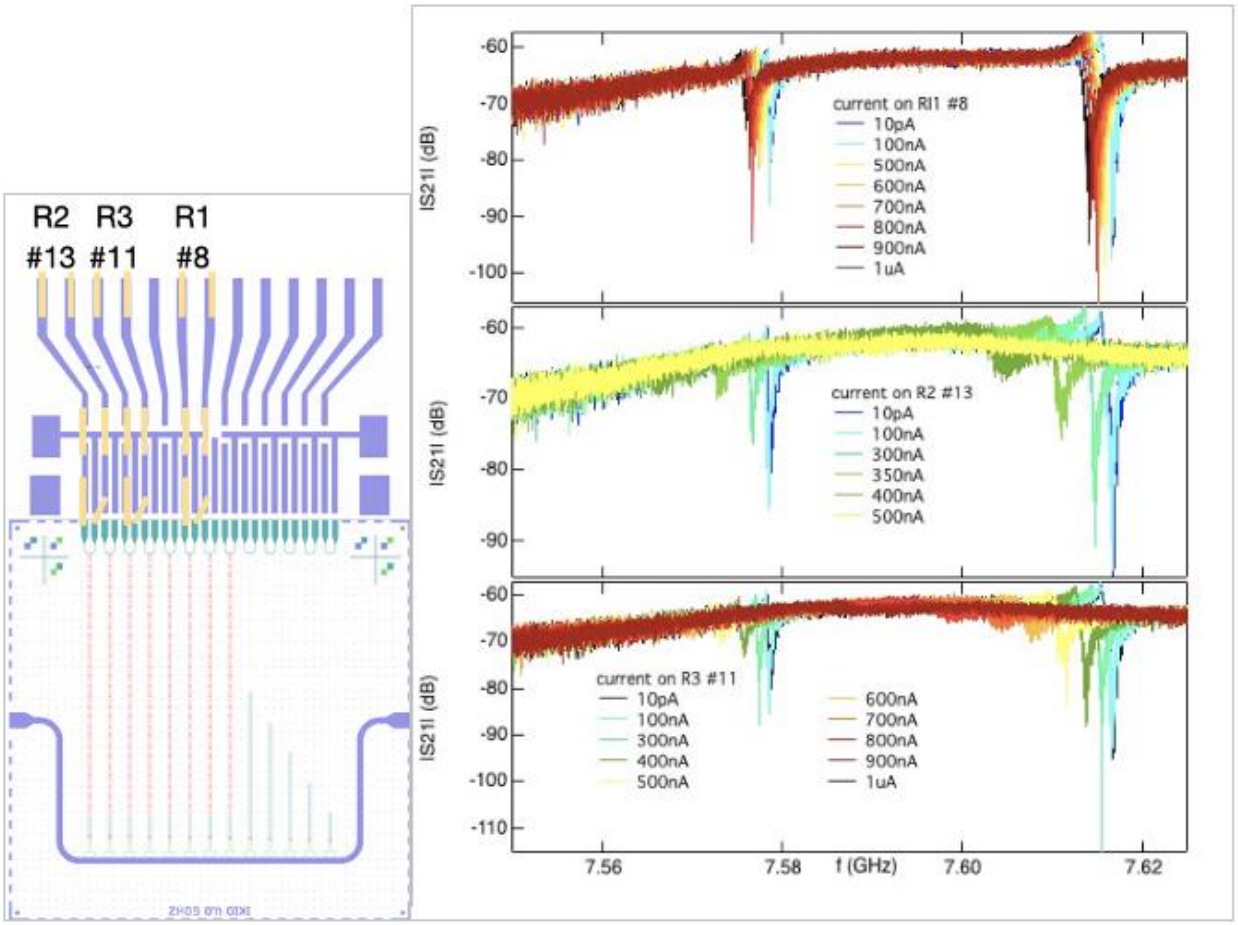

Figure 5.7. Testing of the first iKID prototype (left) with the resonance shifts shown in right.

We observe that the two resonances lying at ~7 GHz shift due to incoming current sent either through R1, R2 or R3 (Fig. 5.7).

The shift is consistent with Joule effect (although not observed on the thermometer) if the resonances are associated with R2 (#13):

- strong influence for current on R2 #13
- less influence for current on R3 #11
- even less influence for current on R1#8

5.4 iKID conclusions and plans

We have elaborated an idea for a possible highly multiplexed readout for the SUPERTED detectors. This readout is based on planar superconducting resonators biased by the DC-like current generated by the TEDs. We have performed extensive EM simulations and designed a prototype. This has been fabricated by our collaborators at KIT and tested in one of the CNRS dilution cryostats. Despite the

This project has received funding from the European Union's Horizon 2020 research and innovation programme under grant agreement No 800923.

still inconclusive results, we demonstrate a first sensitivity of the resonance frequency upon the circulating current. Too many design parameters are degenerate in the first prototype design. We plan thus to simplify the design, and the combination of materials, for the second prototype that will be fabricated and tested in early 2022.

This project has received funding from the European Union's Horizon 2020 research and innovation programme under grant agreement No 800923.

6. Conclusions

We have reported the practical designs, implementation and testing of the readout electronics for a SUPERTED X-ray detector, suitable for the calorimetric measurement mode. Cryogenic setup has been built and modified to accommodate the requirements for the readout electronics. The most appropriate SQUID amplifier electronics were identified and ordered from the vendor, but their planned installation and testing were severely delayed due to the pandemic delays of the delivery of the instruments. In the meantime, we obtained and installed the room temperature electronics, identified an alternative and slightly inferior input SQUID option, and purchased and installed it. It was integrated into the setup in combination with an existing second stage SQUID array and the new room temperature electronics. Performance tests demonstrated the expected good characteristics. In addition, we presented the first practical steps towards an alternative highly multiplexable read-out implementation based on KIDs, intended for the THz bolometer readout.

This project has received funding from the European Union's Horizon 2020 research and innovation programme under grant agreement No 800923.

Bibliography

[1] Z. Geng, A.P. Helenius, T.T. Heikkilä, and I.J. Maasilta, *J. Low Temp. Phys.* **199**, 585 (2020).

[2] J. P. Pekola and J. P. Kauppinen, *Cryogenics* **34**, 10 (1994).

[3] H. W. Ott, "Noise reduction techniques in electronics systems 2nd Ed.", Wiley 1988.

[4] https://vacuumschmelze.com/Company/Quality-and-Safety/Information-for-Manufactured-Articles/CRYOPERM

[5] http://www.cmr-direct.com/en/woven-loom/cmr-cwl-12co-5m

[6] https://www.cryospares.co.uk/GE-Low-Temperature-Varnish-p/c5-101.htm

[7] R. Stolle, "Electromagnetic coupling of twisted pair cables," in *IEEE Journal on Selected Areas in Communications*, vol. 20, no. 5, pp. 883-892, June 2002, doi: 10.1109/JSAC.2002.1007371.

[8] https://www.comsol.com/

[9] J. Clarke and A.I. Braginski, *The SQUID Handbook* , Wiley (2005).

[10] D. Drung, C. Aßmann, J. Beyer, A. Kirste, M. Peters, F. Ruede, and T. Schurig, in *IEEE Trans. Appl. Supercond.* (2007), pp. 699–704.

[11] G.J. Van Nieuwenhuyzen and V.J. De Waal, *Appl. Phys. Lett.* **46**, 439 (1985).

[12] R.P. Welty and J.M. Martinis, *IEEE Trans. Appl. Supercond.* **3**, 2605 (1993).

[13] D. Drung, *Phys. C Supercond. Its Appl.* **368**, 134 (2002).

[14] A. Kher, P. K. Day, B. H. Eom, J. Zmuidzinas, and H. G. Leduc, Kinetic Inductance Parametric Up-Converter, *J. Low Temp. Phys* **184**, 480 (2016).

[15] O. Dupré, A. Benoit, M. Calvo, A. Catalano, J. Goupy,C. Hoarau, T. Klein, K. L. Calvez, B. Sacépé, A. Monfardini, and F. Levy-Bertrand, "Tunable sub-gap radiation detection with superconducting resonators," *Superconductor Science and Technology*, **30**, 045007, (2017).

[16] O. Buisson *et al.*, *Physical Review Letters* **73,** 3153 (1994).

[17] J.N. Ullom, J.A. Beall, W.B. Doriese, W.D. Duncan, L. Ferreira, G.C. Hilton, K.D. Irwin, C.D. Reintsema, and L.R. Vale, *Appl. Phys. Lett.* **87**, 1 (2005).

[18] S. Chakraborty and T.T. Heikkilä, *J. Appl. Phys.* **124**, 123902 (2018).

This project has received funding from the European Union's Horizon 2020 research and innovation programme under grant agreement No 800923.